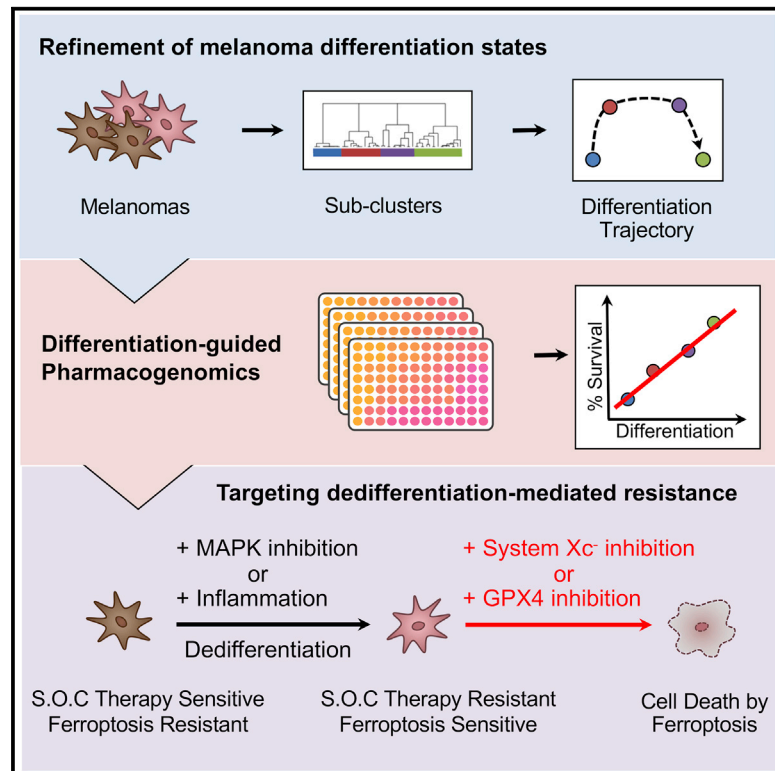


Multi-stage Differentiation Defines Melanoma Subtypes with Differential Vulnerability to Drug-Induced Iron-Dependent Oxidative Stress

Graphical Abstract



Authors

Jennifer Tsoi, Lidia Robert, Kim Paraiso, ..., Nicolaos Palaskas, Antoni Ribas, Thomas G. Graeber

Correspondence

tgraeber@mednet.ucla.edu

In Brief

Tsoi et al. show that melanoma can be categorized into four subtypes following a differentiation trajectory with subtype-specific sensitivity to ferroptosis induction, which presents a therapeutic approach to target the differentiation plasticity to increase the efficacy of targeted and immune therapies.

Highlights

- Melanoma differentiation involves four progressive stepwise states
- Differentiation is two-dimensional with an intermediate neural crest signature
- Melanoma dedifferentiation increases sensitivity to ferroptosis
- Co-targeting ferroptosis can block the dedifferentiation resistance escape route

Multi-stage Differentiation Defines Melanoma Subtypes with Differential Vulnerability to Drug-Induced Iron-Dependent Oxidative Stress

Jennifer Tsoi,^{1,2} Lidia Robert,³ Kim Paraiso,^{1,2} Carlos Galvan,^{1,2} Katherine M. Sheu,^{1,2} Johnson Lay,^{1,2,5} Deborah J.L. Wong,³ Mohammad Atefi,³ Roksana Shirazi,^{1,2} Xiaoyan Wang,⁴ Daniel Braas,^{1,2,5} Catherine S. Grasso,³ Nicolaos Palaskas,^{1,2} Antoni Ribas,^{1,3,6,7} and Thomas G. Graeber^{1,2,5,7,8,9,*}

¹Department of Molecular and Medical Pharmacology, University of California, Los Angeles (UCLA), 570 Westwood Plaza, Building 114, Los Angeles, CA 90095, USA

²Crump Institute for Molecular Imaging, UCLA, Los Angeles, CA 90095, USA

³Department of Medicine, UCLA, Los Angeles, CA 90095, USA

⁴Department of Medicine Statistics Core, UCLA, Los Angeles, CA 90095, USA

⁵UCLA Metabolomics Center, Los Angeles, CA 90095, USA

⁶Department of Surgery, Division of Surgical-Oncology, UCLA, Los Angeles, CA 90095, USA

⁷Jonsson Comprehensive Cancer Center, UCLA, Los Angeles, CA 90095, USA

⁸California NanoSystems Institute, UCLA, Los Angeles, CA 90095, USA

⁹Lead Contact

*Correspondence: tgraeber@mednet.ucla.edu

<https://doi.org/10.1016/j.ccell.2018.03.017>

SUMMARY

Malignant transformation can result in melanoma cells that resemble different stages of their embryonic development. Our gene expression analysis of human melanoma cell lines and patient tumors revealed that melanoma follows a two-dimensional differentiation trajectory that can be subclassified into four progressive subtypes. This differentiation model is associated with subtype-specific sensitivity to iron-dependent oxidative stress and cell death known as ferroptosis. Receptor tyrosine kinase-mediated resistance to mitogen-activated protein kinase targeted therapies and activation of the inflammatory signaling associated with immune therapy involves transitions along this differentiation trajectory, which lead to increased sensitivity to ferroptosis. Therefore, ferroptosis-inducing drugs present an orthogonal therapeutic approach to target the differentiation plasticity of melanoma cells to increase the efficacy of targeted and immune therapies.

INTRODUCTION

Melanoma is a highly aggressive type of skin cancer that arises from melanocytes, the pigment-producing cells of the body. The discovery that approximately half of all melanomas are driven by *BRAF*^{V600} mutations as well as advances in tumor immunology have translated to targeted and immune therapies with impressive response rates and significantly improved

survival (Luke et al., 2017). However, for these treatment modalities there remain patients who do not respond or who ultimately relapse.

Dedifferentiation is a hallmark of cancer progression, and in highly plastic melanoma cells it is a source of cross-resistance to both targeted and immune therapies. This differentiation plasticity can be attributed to the embryonic history of melanocytes, which are derived from the neural crest, a transient, migratory,

Significance

Melanoma cells have the ability to dedifferentiate under cellular stress. This has important therapeutic implications as dedifferentiation contributes to intrinsic and acquired resistance to mitogen-activated protein kinase pathway inhibitors, and occurs as a response to inflammatory signaling during immunotherapy. Therefore, targeting dedifferentiation is a logical approach to strengthen these current therapeutic strategies. Here we categorize melanoma differentiation as four distinct stepwise stages and identify a heightened sensitivity to ferroptosis induction with the degree of differentiation. Our results further define tumor differentiation as an important parameter for patient stratification, and propose a highly orthogonal component to add to standard of care therapeutics, namely enhancing targeted signaling inhibition and immune therapies by synthetic-lethal induction of ferroptosis.

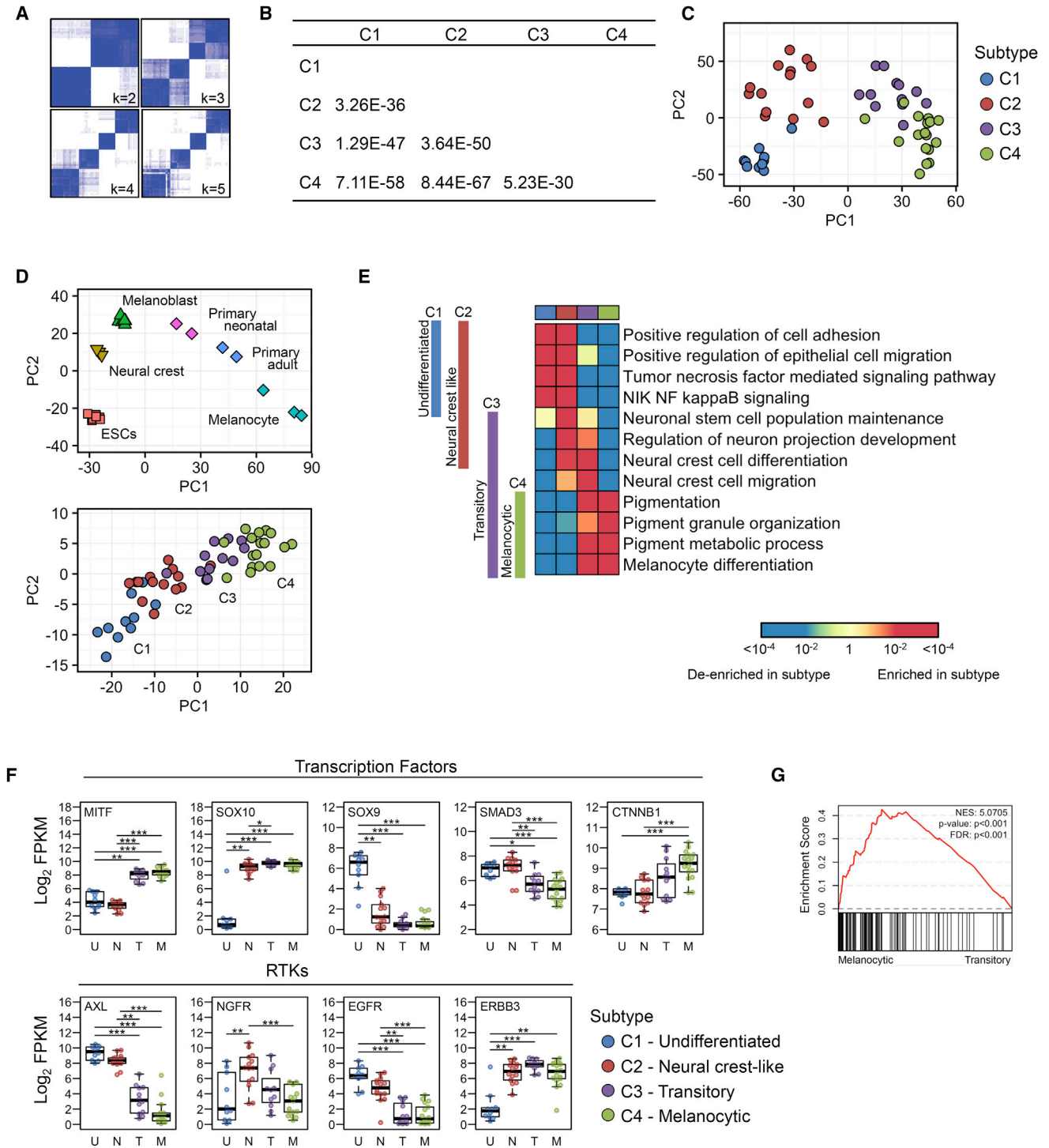


Figure 1. Identification of Four Melanoma Subtypes Related by Progressive Differentiation

(A) Matrix of consensus indices from hierarchical clustering of melanoma cell lines showing differences in clustering stability when grouped from $k = 2$ to $k = 5$ clusters.

(B) Pairwise comparisons showing statistically significant cluster delineations.

(C) PCA of melanoma cell line expression profiles annotated by identified clusters.

(D) PCA of gene expression profiles from an *in vitro* ESC to melanocyte differentiation system (top) and projection of melanoma cell line expression profiles into melanocyte differentiation stage PCA space (bottom).

(E) Heatmap summary of rank-based enrichment analysis p values of each individual cluster versus the remaining clusters in differentiation-associated gene sets. NIK NF, nuclear factor κ B-inducing kinase nuclear factor.

(legend continued on next page)

and multi-potent population of cells that can differentiate into diverse cell types (Sauka-Spengler and Bronner-Fraser, 2008). During acquired resistance to BRAF inhibition (BRAFi), melanoma cells can downregulate MITF, the master regulator of melanocyte differentiation, and upregulate receptor tyrosine kinases (RTKs) such as AXL, EGFR, and PDGFR β (Nazarian et al., 2010; Müller et al., 2014). Low levels of MITF and high levels of AXL are also predictive of intrinsic resistance to mitogen-activated protein kinase (MAPK) pathway inhibition (MAPKi) (Konieczkowski et al., 2014) and have been observed in patient tumors during disease progression on MAPKi therapy (Hugo et al., 2015; Müller et al., 2014; Tirosh et al., 2016). Melanoma cells also dedifferentiate in response to pro-inflammatory signaling, as has been demonstrated in mouse models, which in turn can promote immunotherapy resistance (Landsberg et al., 2012). CD8⁺ T cells isolated from patient tumors were found to frequently recognize melanocyte lineage antigens (Kawakami et al., 2000). Thus, dedifferentiation provides a mechanism to escape immune recognition. In addition, inflammatory MITF-low melanomas were shown to have greater recruitment of myeloid cells (Riesenberg et al., 2015), which could support tumor growth or immune suppression (Hugo et al., 2015; Soudja et al., 2010).

While dedifferentiation could promote resistance to current therapies, we reasoned it might also render cells more susceptible to new vulnerabilities. Cell line pharmacogenomics databases combining genomic information with pharmacological response profiles have helped uncover associations between drug mechanisms of action and molecular subtypes (Seashore-Ludlow et al., 2015; Iorio et al., 2016). Therefore, our goals were to refine our understanding of melanoma differentiation states and use this framework to identify drug vulnerabilities via pharmacogenomics analysis that can be harnessed to overcome the dedifferentiation-based resistance escape route.

RESULTS

Melanoma Subtypes Reflect Four Progressive Differentiation States

We performed consensus hierarchal clustering (Monti et al., 2003) of expression profiles from a panel of 53 human melanoma cell lines, including paired acquired resistance sublines, established from patient biopsies. The results reveal that cell lines fall robustly into four clusters numbered C1–C4 with no appreciable gain in cluster stability when increasing to higher numbers of clusters (Figure 1A and Table S1). We found each cluster to be significantly different from one another using SigClust (Liu et al., 2008) (Figure 1B). In addition, all of the clusters arranged into distinct groups by principal component analysis (PCA) (Figure 1C).

We next investigated how our four melanoma clusters were related by differentiation. We performed a comparative analysis with a human *in vitro* model of melanocyte differentiation (Mica

et al., 2013) where human embryonic stem cells (ESCs) were induced to differentiate sequentially to neural crest, melanoblast, and melanocyte stages. PCA of these differentiation stage gene expression profiles, which included primary melanocytes as a reference, showed that each stage segregated progressively along a two-dimensional arc-like trajectory with differentiation. Projection of the melanoma cell lines onto the same melanocyte differentiation stage-defined PCA space similarly separated out the four identified melanoma clusters, indicating a progressive four-stage differentiation relationship (Figure 1D).

We performed enrichment analysis of each cluster compared with the remaining three and again observed a progressive pattern of differentiation-related enrichment of Gene Ontology (GO) biological process terms (Figure 1E and Table S2). C1 was defined as the undifferentiated subtype due to enrichment for invasive phenotype gene sets such as those involving cell adhesion and migration, in addition to inflammation-related gene sets as observed previously in dedifferentiated MITF-low melanoma cells (Hoek et al., 2006; Konieczkowski et al., 2014). C2 shared enrichment for invasive/inflammation-related gene sets but was defined as the neural crest-like subtype due to its unique enrichment for neural crest-related gene sets. C3 was defined as the transitory subtype, due to concurrent enrichment of neural crest and pigmentation-associated gene sets suggesting a transitional or mixed neural crest to melanocytic state. Finally, C4 is the most differentiated and was defined as the melanocytic subtype, due to loss of a neural crest signature and a strong enrichment for pigmentation-associated gene sets.

We next explored the expression patterns of transcription factors and RTK genes across the identified melanoma subtypes (Figure 1F). As expected, the undifferentiated and neural crest-like subtypes both had low levels of *MITF* and high levels of *AXL*. In addition, *SMAD3* was elevated in these two subtypes, suggesting a role for TGF β signaling with the invasive phenotype as described (Hoek et al., 2006; Rodeck et al., 1999). These two subtypes do have some notable differences. In the undifferentiated subtype, we observed significantly lower levels of *ERBB3*, neural crest marker *NGFR*, and transcription factor *SOX10*. As *SOX10* encodes a critical neural crest lineage-specifying transcription factor essential for melanocyte development (Sauka-Spengler and Bronner-Fraser, 2008), its absence is supportive of an even less differentiated state. Genes upregulated in the undifferentiated subtype include *SOX9* and *EGFR*, the expression of both of which have been shown to be promoted by *SOX10* loss (Shakhova et al., 2012; Sun et al., 2014). This framework highlights that while neural crest markers are associated with dedifferentiated melanomas (Landsberg et al., 2012), there is a subset of even further dedifferentiated melanomas lacking neural crest markers (e.g., *NGFR*[−]), and displaying differential HMG box marker expression (*SOX10*[−], *SOX9*⁺) (Figures 1E and 1F).

The transitory and melanocytic subtypes are more differentiated with higher expression of *MITF* and lower expression of

(F) Boxplots of select transcription factors and RTK genes. Boxplot lines reflect lower quartile, median, and upper quartile. Whiskers reflect 1.5 times above or below the interquartile range, with points outside reflecting outliers. (U, undifferentiated; N, neural crest-like; T, transitory; M, melanocytic. Number in each group: U = 10, N = 42, T = 12, M = 17. Kruskal-Wallis ANOVA and Dunn's post hoc two-tailed test: *p \leq 0.05; **p \leq 0.01; ***p \leq 0.001). FPKM, fragments per kilobase of exon per million fragments mapped.

(G) Analysis of melanocytic (versus transitory) subtype shows enrichment of MITF targets. See also Tables S1 and S2. FDR, false discovery rate; NES, normalized enrichment score.

AXL. Wnt/beta-catenin signaling has been implicated in enhancing MITF target gene expression, and an increased expression of beta-catenin (*CTNMB1*) is observed across these two subtypes in support of a more mature melanocyte signature (Schepsky et al., 2006). To evaluate the differential MITF activity between these two subtypes, we performed enrichment analysis using previously described MITF target genes to infer activity (Hoek et al., 2008). The melanocytic subtype showed stronger enrichment of these MITF target genes (Figure 1G), supportive of greater differentiation.

We next investigated the relationship between our subtypes and the widely appreciated two class “proliferative” and “invasive” phenotypes (Hoek et al., 2006). In the classification by Hoek et al. (2006), there were initially three cohorts (A, B, and C) observed by hierarchical clustering. The strongest transcriptional signatures were found in cohort A and cohort C, which defined the proliferative and invasive phenotypes respectively. We applied the SubMap subtype comparison tool (Hoshida et al., 2007) between the two datasets and found our identified clusters (C1–C4) show informative mapping relationships for all cohorts identified by Hoek et al. (2006), with C4 mapped to cohort A, C3 to both cohorts A and B, and C2–C1 to cohort C (Figure S1A). Thus, our subtypes are congruent with the Hoek classification, refining each of the proliferative and invasive classifications into two further subgroups, and providing a 4-stage stepwise differentiation context based on normal melanocyte differentiation programs. This refinement involves the emergence of a second transient transcriptional program that first turns on (increase in PC2 genes) and then off during melanoma (and melanocyte) differentiation transitions (Figures 1C and 1E) and is thus reminiscent of other transient developmental transcriptional programs (Spitz and Furlong, 2012; Telley et al., 2016).

Four-Stage Differentiation Model Reflects Treatment-Induced Stepwise Dedifferentiation

Since melanoma cells are highly plastic and can dedifferentiate in response to MAPKi and pro-inflammatory signaling from immunotherapy, we sought to relate these treatment-induced differentiation transitions to our subtypes. We first defined specific transcriptional signatures that distinguish each subtype by differential expression (Table S3). In addition, we tested the extent of shared differentially expressed genes between “adjacent” subtypes compared with other subtype pairings. Consistent with our interpretation of the subtypes as four progressive differentiation states, the only pairings that generated an appreciable signature were between sequential clusters in the two-dimensional arc-like trajectory model (Figures S1B and S1C).

We applied these signatures to investigate RTK-upregulated, dedifferentiation-associated acquired resistance to MAPK pathway inhibitors (Müller et al., 2014). To quantify the degree of treatment-induced dedifferentiation, we calculated a differentiation trajectory position score for each sample using a “center of mass” approach that reflects the relative position along the differentiation trajectory where the sample has the strongest gene expression signature match (STAR Methods). The difference in the score between each sample from its respective control thus represents the magnitude and direction of change in differentiation. In the BRAF mutant cell lines M229P and

M238P, we observed that cell lines begin with different initial differentiation stages as defined by their subtype signatures, but shift notably toward the undifferentiated signature upon acquired resistance to vemurafenib (M229R, M238R) (Figure 2A). Similar results were observed from analysis of an independent study of RTK-driven single- and double-drug (BRAFi and MEKi)-resistant cell lines (Figure S1D). As a negative control, resistance mediated by genomic alterations that directly reactivate the MAPK pathway, such as through *NRAS* mutation (M249R) or *BRAF* alternative splicing (M395R, M397R), do not show differentiation changes (Figure 2A) (Nazarian et al., 2010).

To evaluate the temporal changes that occur with the acquisition of resistance, we performed a vemurafenib treatment time-course study using the M229 parental cell line, which starts as a transitory subtype but switches to an undifferentiated subtype in M229R. Supportive of our differentiation model, treatment with vemurafenib produced gene expression changes with time that marked progressive dedifferentiation through our subtype signatures toward the undifferentiated subtype (Figures 2B and 2C). Similar temporal changes toward dedifferentiation were observed in an additional melanoma cell line, M397. This line was tested because reported resistant sublines of M397 (M397R) occurred through *BRAF* alternative splicing (Poulikakos et al., 2011), a resistance mechanism that re-activates the MAPK pathway, and have the same differentiation state as their parental line (Figure 2A). Together, these observations support that dedifferentiation and MAPK-reactivation routes of BRAF resistance are not mutually exclusive. In some cases, dedifferentiation can be a transient response of adaptive resistance (Fallahi-Sichani et al., 2017; Sun et al., 2014; Titz et al., 2016) and provides a reservoir of cells allowing for expansion or evolution of resistant clones with genetic mechanisms that enable return to the parental differentiation state (Ramirez et al., 2016). In alternate cases, the dedifferentiation state can be stabilized, such as through loss of *SOX10* by epigenetic reprogramming (Shaffer et al., 2017).

Within the heterogeneity of patient tumors, our subtype signatures were able to detect dedifferentiation both during treatment and upon disease progression following double-drug MAPK therapy (Figures S1E and S1F) (Kwong et al., 2015; Tirosh et al., 2016). In addition, across a large panel of MAPK inhibitor disease progression tumors with diverse and heterogeneous resistance mechanisms (Hugo et al., 2015), our trajectory position metric distinguishes dedifferentiation-associated resistance mechanisms from those involving MAPK re-activation (Figure S1G).

We next applied the subtype signatures to investigate immunotherapy resistance occurring through inflammation-induced dedifferentiation. Such dedifferentiation has been shown to occur *in vivo* in a mouse model of adoptive cell transfer using transgenic cytotoxic T cells targeting the melanocytic antigen gp100 (Landsberg et al., 2012). In this model, dedifferentiation decreased tumor antigen presentation, as scored by loss of melanocytic biomarkers (gp100, TRP2), and resulted in tumor progression. As expected, we observed greater expression of dedifferentiation signatures within the relapse group compared with the control both in the tumors and in tumor-derived cell lines (Figure 2D). Collectively, these results demonstrate that our differentiation framework is consistent with and can

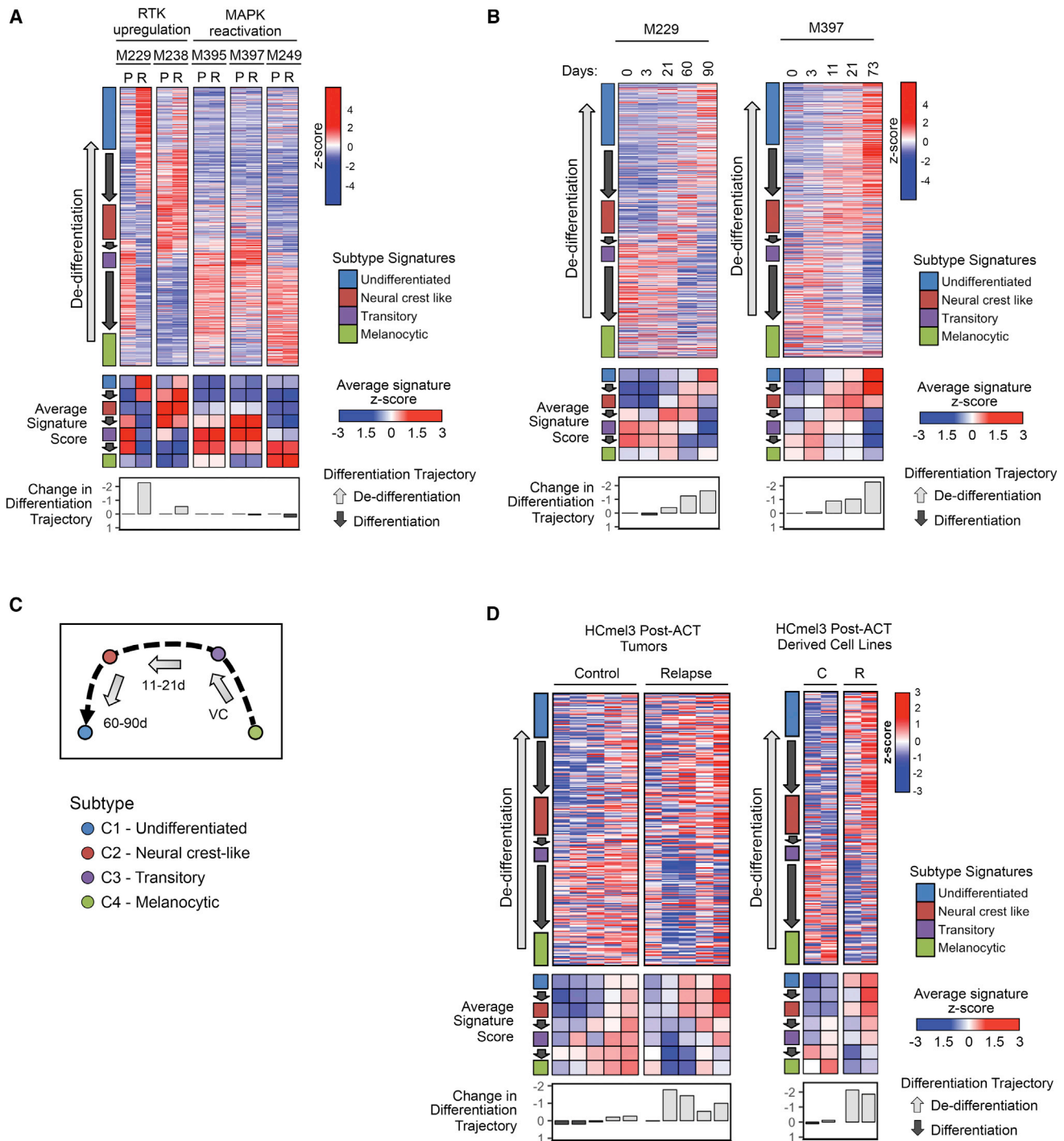


Figure 2. Treatment-Induced Dedifferentiation in the Context of the Four-Stage Differentiation Model

(A and B) Heatmap of signature genes, average signature Z scores, and differentiation trajectory position changes for matched parental and resistant cell lines (A) and for a vemurafenib treatment time course in M229 and M397 melanoma cell lines compared with DMSO vehicle control (0 days treatment) (B).

(C) Schematic representing progressive dedifferentiation along the two-dimensional trajectory model with increased time under vemurafenib treatment.

(D) Heatmap of signature genes, average signature Z scores, and differentiation trajectory position changes for murine HCmel3 tumors or cell lines with treatment control or relapse from adoptive transfer of antigen specific T cells. (C, control; R, relapse). Dark gray arrows represent increased differentiation state and the light gray arrow indicates the treatment-induced dedifferentiation direction. See also [Figure S1](#) and [Table S3](#).

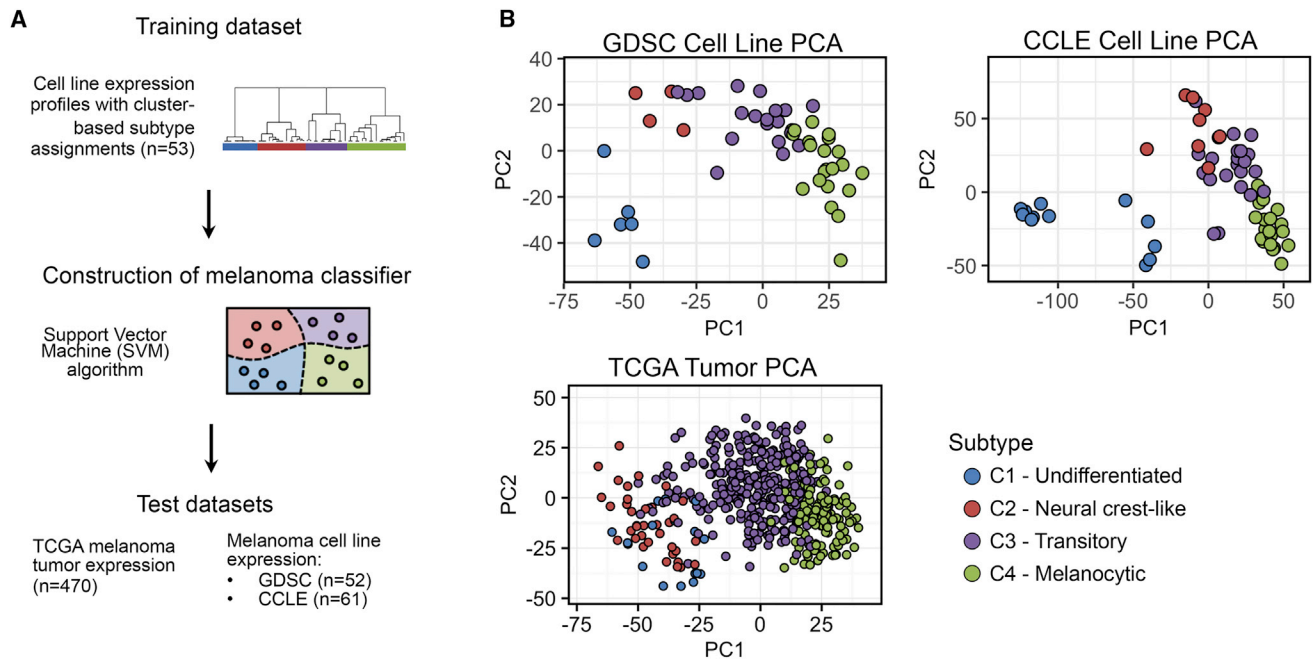


Figure 3. Melanoma Classifier Identifies Consistent Subtypes in Cell Lines and Tumors

(A) Schematic of the melanoma subtype classifier pipeline.

(B) PCA of GDSC, CCLE, and TCGA datasets annotated by the cluster prediction assignment. For the TCGA dataset, immune- and keratin-associated genes were removed to provide melanoma cell-specific analysis. See also [Figures S2, S3, and S4](#), and [Table S4](#).

semi-quantitatively reflect dedifferentiation associated with melanoma standard of care therapy resistance.

Melanoma Classifier Identifies Consistent Subtypes in Cell Lines and Tumors

Dedifferentiation responses to both MAPKi and to immunotherapy suggest that targeting the dedifferentiated state is a viable approach to overcome resistance. As our multi-stage subtypes provide a refinement of melanoma differentiation, we built a predictive model trained on our cell line expression profiles to predict differentiation subtypes of cell lines profiled in publicly available pharmacogenomics resources ([Figure 3A](#)). We applied our prediction model to the Cancer Cell Line Encyclopedia (CCLE) and Genomics of Drug Sensitivity in Cancer (GDSC) independent datasets. PCA of each dataset annotated by the prediction results showed differentiation trajectory patterns similar to our initial analysis ([Figure 3B](#)), further supporting the robustness of the four-step differentiation framework.

To evaluate the relevance of the subtypes in patient tumors, we extended our cell line-trained classifier to The Cancer Genome Atlas (TCGA) skin cutaneous melanoma (SKCM) bulk tumor expression profiles ([Table S4](#)). We evaluated the similarity of gene expression between the cell lines and bulk tumors by comparing the maximum expression of each gene and observed strong concordance ($R = 0.87$), confirming that cell lines do retain tumor-relevant expression patterns ([Figure S2A](#)). The residual disparity is mostly from non-melanoma cells within the tumor bulk, such as from immune cells (immune-specific CD markers and cytokines) and adjacent normal tissue (epidermis-specific

keratin gene pairs KRT1/10 and KRT5/14) ([Moll et al., 2008](#)). When we removed these two confounding signatures ([Figure S2B](#), [STAR Methods](#)), PCA of the bulk tumor expression profiles showed analogous arc-like trajectory differentiation subtype patterns consistent with the pure cell line cases ([Figure 3B](#)). Similar patterns were also observed in a parallel approach where we projected the tumor profiles onto the cell line-defined PCA space, which emphasizes melanoma-specific genes and reduces the influence of non-melanoma cell genes within the tumor ([Figures S2C and 1C](#)).

Across all datasets, we observed subtype signature profiles, RTK and transcription factor expression patterns, and inferred MITF activity consistent with our original cell line analysis ([Figures S3A–S3D](#)). As TCGA tumor and GDSC cell line profiles have matching methylation data, we explored the extent that differentiation-associated expression differences could be regulated at the methylation level. Our analysis of cell lines and tumors revealed that promoter methylation beta values are inversely correlated with expression for *AXL*, *MITF*, *SOX10*, *SMAD3*, and *CTNNB1* ([Figure S4A](#)). Furthermore, PCA of the genome-wide promoter methylation data within the GDSC dataset revealed a similar arc-like differentiation subtype trajectory as in the expression-based analysis ([Figure S4B](#)). These results match the generally expected trend for methylated promoters to inhibit transcription and are supportive of epigenetic regulation of differentiation as previously appreciated ([Lauss et al., 2015](#); [Shaffer et al., 2017](#)). Collectively, these results demonstrate the consistency of these subtype relationships detectable in both melanoma cell line and tumor cohorts independently.

Pharmacogenomics Integration Reveal Inverse Relationship between Differentiation State and Sensitivity to Ferroptosis-Inducing Drugs

We next applied our prediction of subtypes of the CCLE and GDSC datasets to explore matching drug sensitivity profiles available from the pharmacogenomics-based Cancer Therapeutics Response Portal (CTRP) (Seashore-Ludlow et al., 2015). We first filtered for drugs that exhibited subtype-specific sensitivity (ANOVA $p < 0.01$) and performed hierarchical clustering to identify drug clusters with a similar mechanisms of action. An interrogation of the screened compounds revealed that with increased dedifferentiation status there was an increased sensitivity to all ferroptosis-inducing drugs ($n = 4/4$) (Figures 4A and S5A). Using our defined differentiation trajectory score to quantify the relative differentiation between samples, the relationship between dedifferentiation and sensitivity was significantly correlated for all compounds (Figure 4B). The ferroptosis-inducing compounds include erastin, (1S, 3R)-RSL3, ML162, and ML210. Ferroptosis occurs through an iron-dependent accumulation of lethal lipid reactive oxygen species (ROS) and is regulated by GPX4, a glutathione-dependent enzyme that catalyzes the reduction and detoxification of lipid ROS (Dixon et al., 2012; Yang et al., 2014). Compounds (1S, 3R)-RSL3 (hereafter referred to as RSL3), ML162, ML210 induce ferroptosis by direct inhibition of GPX4, while erastin indirectly inhibits GPX4 further upstream through depletion of glutathione by targeting the System Xc⁻ transporter (Dixon et al., 2012; Yang et al., 2014). In contrast, we did not observe subtype-specific sensitivity in the subclass of ROS-inducing drugs that do not induce ferroptosis (Figure S5B).

We next sought to verify these differentiation-associated pharmacogenomic sensitivity trends in the context of our melanoma cell lines. Consistent with the CTRP findings, sensitivity to the ferroptosis-inducing drugs erastin and RSL3 was highly correlated with dedifferentiation (Figures 4C and 4D). In the order of progressive dedifferentiation there was an increase in sensitivity: the melanocytic subtype cell lines were more resistant to both drugs, the transitory and neural crest-like subtype lines were moderately sensitive, and the fully undifferentiated subtype cell lines were highly sensitive. Overall, the trend for increased ferroptosis sensitivity with dedifferentiation had strong statistical significance ($p = 10^{-12}$, Figure 4).

Furthermore, therapy-induced dedifferentiation with long-term BRAF inhibitor treatment or upon acquired resistance generally resulted in an increase in ferroptosis sensitivity upon both erastin and RSL3 treatment (Figures 4E and 4F). SKMEL28R cells were a partial exception in that they demonstrated increased sensitivity to RSL3 but not erastin. The increased sensitivity to the GPX4 inhibitor RSL3 supports that these cells are more sensitive to ferroptosis than their parental line. In this case, the differences between erastin and RSL3 sensitivity could be attributed to their upstream versus downstream targets of ferroptosis induction. Factors such as those affecting the ability of erastin to inhibit its upstream System Xc⁻ target or the ability of cells to compensate for cystine/glutathione depletion could reverse erastin sensitivity without modulating RSL3 sensitivity. As a negative control, M249R, which achieves resistance through acquisition of an NRAS mutation with no change in differentiation status (Figure 2A), was as insensitive to ferroptosis induction as its parental

line (Figures 4E and 4F). As an additional negative control, treatment with piperlongumine, an ROS-inducing drug that triggers apoptosis (Raj et al., 2011) rather than lipid ROS-mediated ferroptosis, did not show differentiation-associated sensitivity (Figures S5B and S5C). Taken together, these results support that lipid peroxide sensitivity is influenced by melanoma differentiation state.

Next, we sought to confirm that the observed drug-induced cell death occurred via ferroptosis in melanoma as previously characterized in other cancer types (Dixon et al., 2012; Yang et al., 2014). Death induced by erastin treatment in the undifferentiated signature cell lines M296, M410 M229R, and M238R, occurred rapidly within 12 hr (Figure S6A). This decrease in cell viability was almost completely rescued either by iron chelation via deferoxamine (DFO) or by the lipophilic antioxidant Trolox (Figures 5A and S6A), demonstrating that cell death is both iron and ROS dependent, respectively. The mechanism of erastin-induced cell death is distinct from apoptosis, as treatment with the pan-caspase inhibitor Z-VAD-FMK could not rescue death induced by erastin treatment but could rescue apoptosis induced by staurosporine as a positive control (Figure S6B). Furthermore, we observed a high induction of lipid ROS at a time preceding cell death (10 hr) in erastin-sensitive cell lines, which was not present in the non-sensitive lines tested (Figures 5B and S6C). This increase in lipid ROS could be rescued by DFO treatment, further indicating that cell death occurs through the iron-dependent accumulation of lipid ROS. At the same time point post-treatment, cytosolic ROS was found to be elevated in all cell lines but at substantially higher levels in the undifferentiated signature cell lines. This increase in cytosolic ROS was iron dependent and was reduced by DFO treatment (Figures 5C and S6D).

To test whether the differences in ROS levels in the less sensitive cells were due to the inability of erastin to deplete glutathione, we measured glutathione by mass spectrometry in isogenic sublines M229P and M229R, and M238P and M238R (Figure S6E and Table S5). Erastin treatment significantly depleted both reduced glutathione (GSH) and oxidized glutathione (GSSG) across all the cell lines (Figures 6A and 6B). However, the erastin-sensitive M229R and M238R sublines had lower basal levels of GSH and GSSG, and also exhibited a greater fold-change decrease with treatment compared with their respective parental lines. We confirmed that basal levels of GSH in the vemurafenib-resistant cell lines were significantly lower than in paired parental cell lines using the Ellman's reagent-based glutathione quantitation assay (Figure 6C). Expanding this assay to additional lines, we found levels of GSH to be significantly correlated to the degree of dedifferentiation (Figure 6C). Supplementation of the culture medium with GSH substantially rescued both erastin- and RSL3-induced cell death (Figure 6D), confirming glutathione levels as a mechanistic link between sensitivity to ferroptosis-inducing drugs and differentiation state.

Combination Treatment with Ferroptosis-Inducing Drugs Is Effective Against Treatment-Induced Dedifferentiation and Resistance

Ferroptosis-inducing drugs were initially discovered from an RAS synthetic-lethal screen and studies have shown a

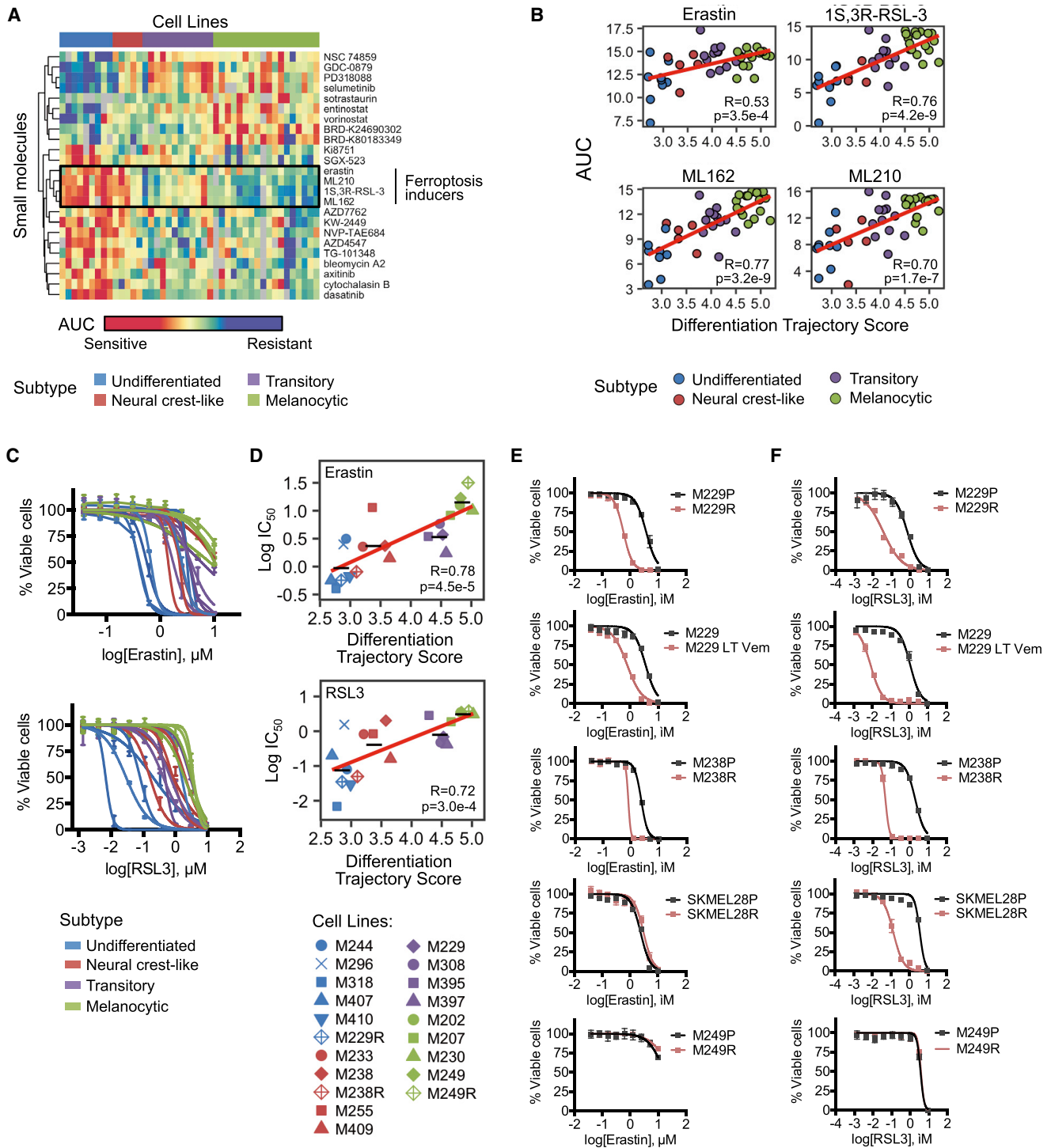


Figure 4. Integration of Pharmacogenomics Drug Sensitivity Profiles Reveals Subtype-Specific Sensitivity to Ferroptosis-Inducing Drugs

(A) Hierarchical clustering of the CTRP pharmacogenomics database area under the curve (AUC) values across differentiation subtypes.
 (B) Plot of AUC values versus the differentiation trajectory score for all ferroptosis-inducing drugs from the CTRP. Low AUC values indicate increased sensitivity.
 (C) Dose-response curves across indicated M-series melanoma cell lines for erastin and RSL3.
 (D) Corresponding plot of $\log \text{IC}_{50}$ (half maximal inhibitory concentration) concentration values for erastin and RSL3 treatment versus the differentiation trajectory score. Black dashes indicate mean within the subtype group.
 (E and F) Dose-response curves showing increased sensitivity to erastin (E) and RSL3 (F) in cell lines with vemurafenib-induced dedifferentiation including both acquired resistance lines (P, parental; R, resistant) or long-term (LT) adaptive resistance (44 days). Percentages of viable cells are calculated relative to DMSO. Drug response curves are shown as mean \pm SEM of two replicates and are representative of at least three independent experiments. See also [Figure S5](#).

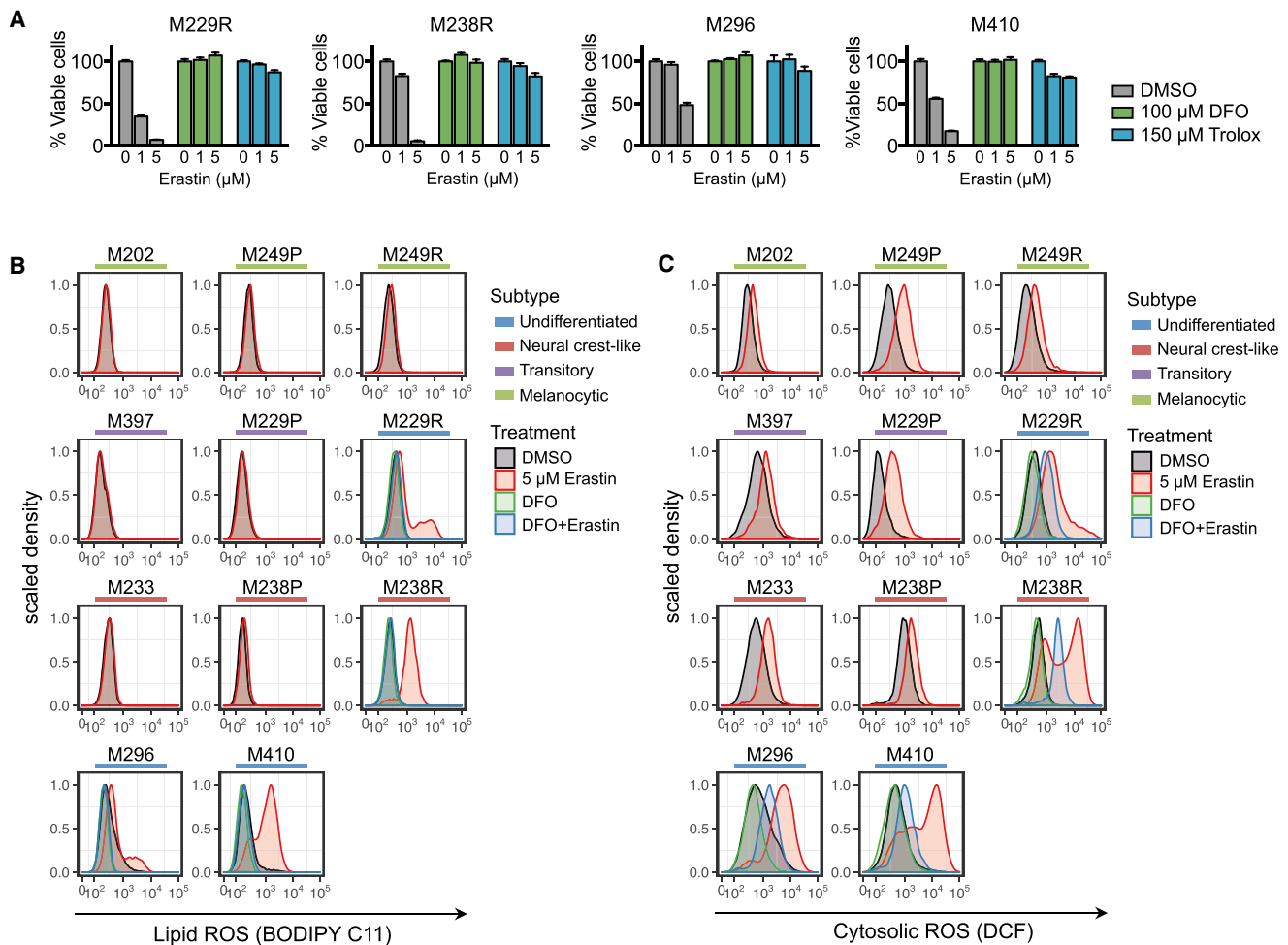


Figure 5. Erastin Treatment Induces Ferroptosis in Dedifferentiated Melanoma Cells

(A) Measurement of percent viable cells compared with DMSO control with erastin treatment alone or in combination with DFO or Trolox. Data shown represent mean \pm SEM of three replicates, and are representative of at least three independent experiments.

(B and C) ROS measurements after 10 hr erastin treatment across cell lines by flow cytometry using BODIPY-C11 probe to measure lipid ROS (B) and CM-H2DCFDA probe to measure cytosolic ROS (C). See also Figure S6.

dependence on MAPK signaling for ferroptosis in some contexts (Yang and Stockwell, 2008; Yagoda et al., 2007). We first examined phospho-ERK levels across the melanoma cell line panel and did not observe any subtype-specific patterns associated with sensitivity to ferroptosis (Figure S7A). To evaluate the feasibility of combination treatment to overcome BRAF inhibitor resistance, we confirmed that the presence of vemurafenib does not reduce the high lethality from ferroptosis induction in dedifferentiated, vemurafenib-resistant cell lines. As expected, vemurafenib treatment alone was effective in reducing the viability of parental cell lines M229P and M238P but had little effect on vemurafenib-resistant lines M229R and M238R. On the other hand, treatment with erastin in the dedifferentiated M229R and M238R lines resulted in a substantial loss of viable cells that was not attenuated even in the presence of high concentrations of vemurafenib (Figure 7A). This result confirmed that there is no drug antagonism between BRAF inhibition and erastin in these dedifferentiated melanoma cells.

Ferroptosis-inducing drugs and BRAF inhibitors optimally target melanoma cells at distinct differentiation stages. Since dedifferentiation is an adaptive response to BRAF inhibition, we sought to directly test the efficacy of combining ferroptosis-inducing drugs with BRAFi against a cohort of BRAF mutant melanomas. We evaluated the effects of combination treatment on three melanoma cell lines that are initially BRAFi sensitive but become resistant due to dedifferentiation. Biomarker evaluation of persisting cells after long-term vemurafenib treatment (21 days) showed upregulation of AXL and NGFR, and downregulation of MITF or its target gene MART-1, confirming their inhibitor-induced dedifferentiation (Figure 7B). Of note, at this prolonged treatment time point, pERK levels rebounded likely due to feedback mechanisms that have previously been observed to begin within a few days during MAPK inhibition (Figure S7B) (Lito et al., 2012; Paraiso et al., 2010). Importantly, inclusion of erastin or RSL3 with vemurafenib in the treatment protocol resulted in a substantial decrease in long-term persisting cells (16–24 days) (Figures 7C and S7C–S7E).

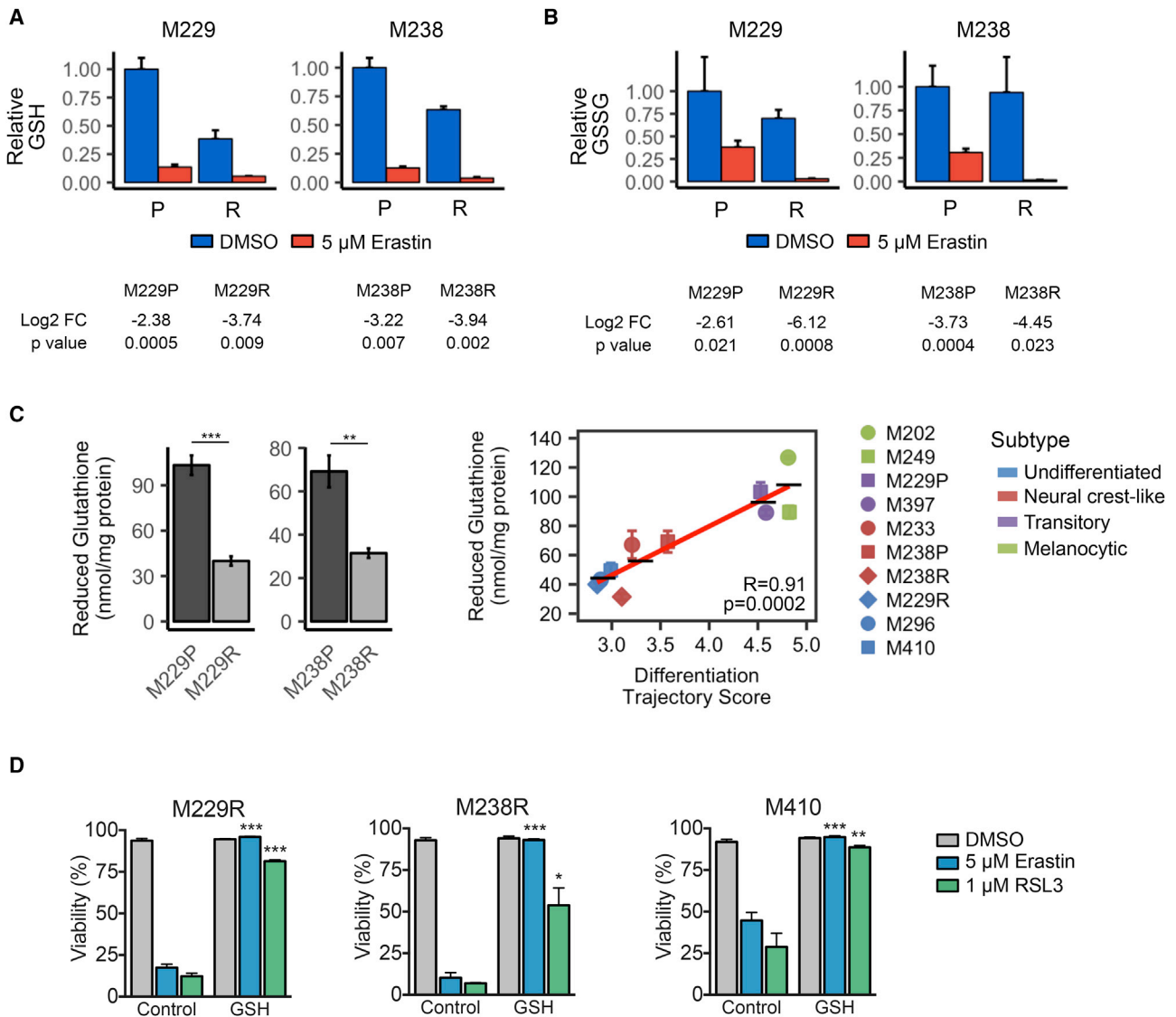


Figure 6. Lower Basal Levels of Glutathione in Dedifferentiated Melanoma Increase Sensitivity to Ferroptosis Induction

(A and B) Relative amounts of GSH (A) and oxidized GSSG (B) measured by mass spectrometry-based metabolomics after 8 hr erastin treatment compared with untreated parental control for the indicated isogenic cell lines. (P, erastin-insensitive parental cell lines; R, erastin-sensitive BRAF_i-resistant cell lines).

(C) Barplot of GSH levels measured by Ellman's reagent of the isogenic cell line pairs (left). GSH levels versus the differentiation trajectory score across panel of melanoma cell lines (right). Data shown represent mean \pm SEM of three independent experiments. ** $p \leq 0.01$; *** $p \leq 0.001$. Subtype group means indicated by black dashes (right).

(D) Trypan blue exclusion viability assay of 24 hr erastin or RSL3 treatment with or without supplementation of 5 mM GSH in the culture medium. Data shown represent mean \pm SEM of three independent experiments. One-tailed t test: * $p \leq 0.05$; ** $p \leq 0.01$; *** $p \leq 0.001$. See also [Figure S6](#) and [Table S5](#).

An inflammatory microenvironment from elevated immune activity can also promote dedifferentiation of melanoma cells. Therefore, we next sought to test whether immunotherapy-associated, cytokine-induced dedifferentiation would cause melanoma cells to become more sensitive to ferroptosis-inducing drugs. The dedifferentiation response of melanoma cells to pro-inflammatory signaling can be replicated *in vitro* by treating cell lines with T cell secreted cytokines such as tumor necrosis factor alpha (TNF α) and interferon gamma (IFN γ) (Landsberg et al., 2012; Natarajan et al., 2014). We first confirmed that TNF α and IFN γ stimulation resulted in activation of the nuclear

factor κ B (NF- κ B) or STAT1 signaling pathways, respectively (Figures S7F and S7G) and induced dedifferentiation, as determined by upregulation of AXL and decreased levels of MITF or its target gene MART-1 (Figure 7D). The degree of signaling activation and dedifferentiation was most prominent with IFN γ across all cell lines, and for TNF α in cell lines M229 and M397. Consistent with the dedifferentiation response, treatment with erastin or RSL3 under cytokine stimulation resulted in increased cell death compared with cytokine-only or untreated cells (Figures 7E and S7H-S7J). M249 did not exhibit increased cell death with TNF α treatment alone or when combined with ferroptosis-

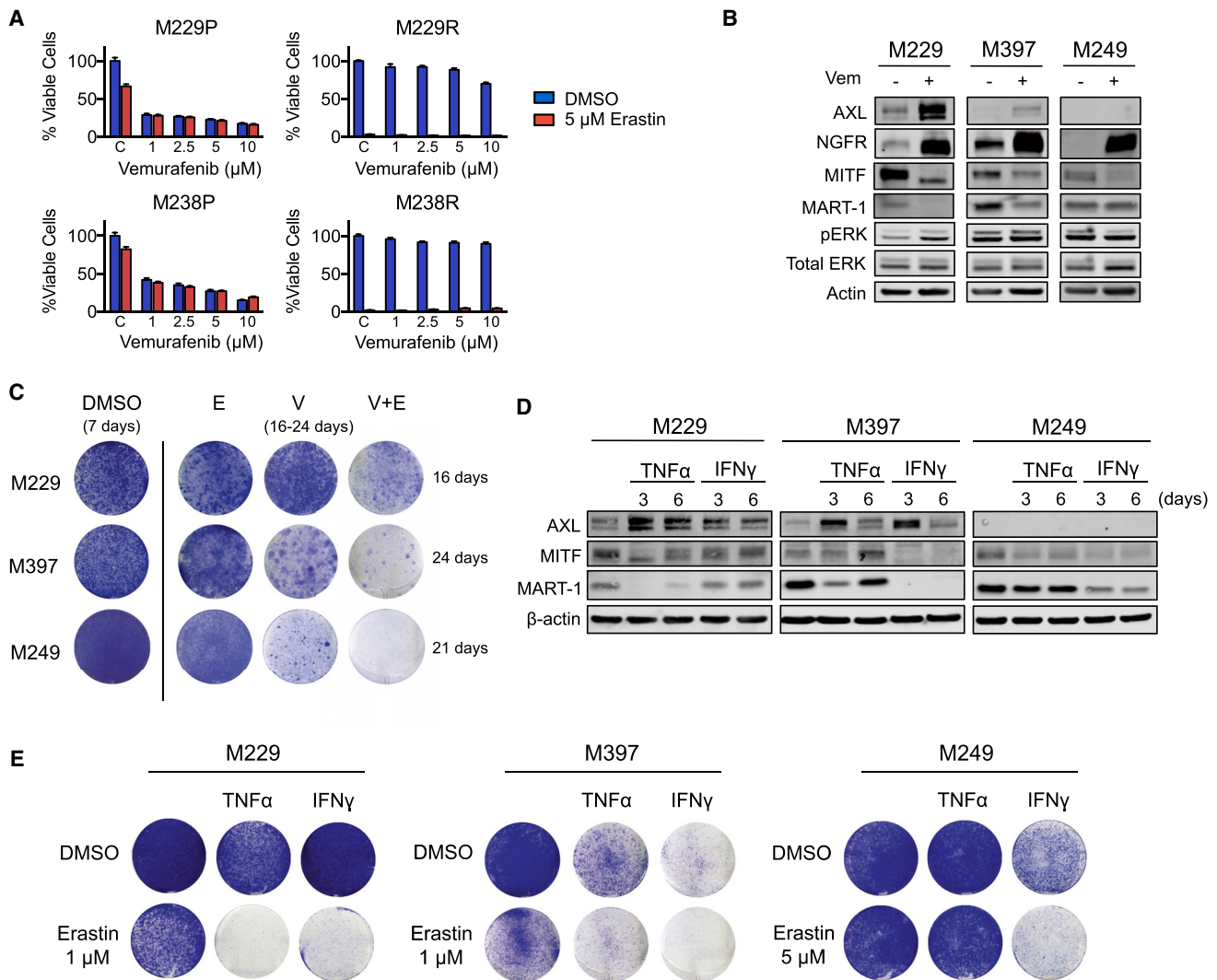


Figure 7. Reduction in Persistent Dedifferentiated Melanoma Cells upon Combination Treatment with Ferroptosis-Inducing Drugs

(A) Measurement of percentage of viable cells compared with vehicle control (DMSO) of erastin treatment combined with increasing concentration of vemurafenib for 72 hr. Data shown in barplots represent mean \pm SEM of three replicates.
 (B) Immunoblots of differentiation and signaling markers in cell lines treated with long-term (21 days) vemurafenib treatment.
 (C) Crystal violet staining assays of long-term combination treatment of erastin (E = 2 μ M for M229 and M397, 5 μ M for M249) and vemurafenib (V = 1 μ M) for 16 days (M229), 24 days (M397), or 21 days (M249). DMSO treated cells were stained when confluent (7 days).
 (D) Immunoblots of cell lines treated with the indicated cytokines.
 (E) Crystal violet staining assays of erastin treatment for 7 days with cytokine exposure for the initial 3 days (M229 and M249) or 7 days (M397). Interferon gamma (IFN γ) = 100 U/mL, TNF α = 1,000 U/mL. Data shown are representative of three independent experiments. See also [Figure S7](#).

inducing drugs, consistent with a muted signaling activation by TNF α in this line ([Figure S7F](#)). However, we did observe modest biomarker-based dedifferentiation upon IFN γ cytokine treatment in M249 cells, and accordingly observed increased sensitivity under higher doses of ferroptosis-inducing drugs (5 μ M erastin, 500 nM RSL3). In these experiments, the combined treatment contributed substantially and in some cases in a synthetic-lethal fashion to reduce any persisting cell population. Further relevance for such a dual-targeting approach comes from the observation that melanoma cells can upregulate surface expression of the PD-L1 ligand in response to IFN γ to suppress T cell function through activation of inhibitory PD1

receptor signaling ([Iwai et al., 2002](#); [Taube et al., 2012](#)). Therefore, reducing this dedifferentiated persisting population of cells via their sensitivity to ferroptosis induction can potentially boost overall anti-tumor immunity by preventing an accumulation of melanoma cells with immunosuppressive capabilities.

DISCUSSION

Multiple studies have shown that melanoma cell lines and tumors can be consistently categorized into two phenotypes with divergent transcriptional profiles related to differentiation. Our results expand these two phenotypes into four subtypes that

reflect distinct and progressive differentiation states found across multiple independent tumor and cell line datasets. Further supporting this differentiation trajectory framework is the observation that melanoma cells can dedifferentiate progressively through these subtype signatures with elapsed time under BRAF inhibitor treatment and accompanying acquisition of BRAFi resistance. We found that progression along the dedifferentiation trajectory is observed in patient samples on standard of care melanoma kinase inhibitor therapies and in mouse models of cancer immunotherapy.

Pharmacogenomic analysis with our refined differentiation framework revealed an association between sensitivity to ferroptosis and the degree of dedifferentiation, where the undifferentiated subtype was the most sensitive and the melanocytic subtype the most resistant. This sensitivity pattern has therapeutic implications, and our experiments support the efficacy of ferroptosis-inducing drugs in targeting both innate resistance and acquired dedifferentiation-associated resistance induced by kinase therapies and by immunotherapy-associated cytokines. Therefore, up-front combination therapies that include ferroptosis-inducing drugs have the potential to enhance current treatment options for melanoma patients by providing a synthetic-lethal approach to kill the persistent melanoma cell populations. Dedifferentiation-based adaptation can be seen in patient biopsies in as little as 1 to 3 weeks (Kwong et al., 2015). This early adaptation time frame argues for up-front co-treatment, which has generally been found to be more efficient than sequential therapy (Eroglu and Ribas, 2016). Up-front co-targeting would furthermore prevent cells from accumulating additional therapy-confounding genomic alterations such as *NRAS* mutations or *BRAF* amplifications.

It was recently demonstrated that a mesenchymal or persister cell state is highly dependent on GPX4 peroxidase activity for survival, highlighting the potential for co-treatment with GPX4 inhibitors to overcome epithelial-mesenchymal transition (EMT)-related resistance mechanisms (Hangauer et al., 2017; Viswanathan et al., 2017). These results are in line with our findings as low MITF melanoma cells do exhibit mesenchymal-like expression patterns and phenotype (Li et al., 2015). However, melanocytes are not from the epithelial lineage. During malignant transformation to melanoma, distinct sets of embryonic EMT family transcription factors are expressed at each stage, even in the most differentiated MITF-positive state (Caramel et al., 2013; Denecker et al., 2014).

Melanocytes have vital antioxidant stresses and defenses inherent to their biology, owing to the high oxidative stress from melanin biosynthetic processes and UV radiation (Denat et al., 2014). Thus, it is conceivable that the loss of differentiation programs that combat redox stresses could render redox-challenged cancer cells susceptible to oxidative stress. High MITF cells were found to be more resistant to H₂O₂-induced cell death through MITF transcriptional upregulation of the redox sensor APE-1 (Liu et al., 2009). MITF has also been shown to drive the expression of PGC1 α , a key transcription factor regulating mitochondria biogenesis and expression of ROS detoxifying enzymes (Vazquez et al., 2013). Notably, both in the pharmacogenomics data and in our confirmation experiments, sensitivity to drug-induced lipid redox stress was more distinct between differentiation states than was sensitivity to other categories of

drug-induced redox stress. In addition to GSH levels, differential levels of cellular iron, iron-dependent lipoxygenases, and oxidizable polyunsaturated fatty acids in the lipid membrane could all contribute to the differences in ferroptosis sensitivity (Dixon et al., 2012; Yang et al., 2016).

Metastasizing melanoma cells have been shown to experience increased oxidative stress, with successful metastasis dependent on increased GSH regeneration (Piskounova et al., 2015). Thus, metastasizing cells could be more sensitive to ferroptosis, and treatment with ferroptosis-inducing drugs may potentially limit metastasis. Characterization of the *in vivo* efficacy of ferroptosis-inducing compounds is currently limited by lack of compounds with sufficient bioavailability (Viswanathan et al., 2017; Hangauer et al., 2017). However, genetic experiments using *GPX4* knockout melanoma cells have demonstrated that increased ferroptosis sensitivity observed *in vitro* can be recapitulated *in vivo* either alone or in combination with BRAF inhibition (Viswanathan et al., 2017; Hangauer et al., 2017).

In summary, our refined framework of multi-stage melanoma differentiation subtypes guided the discovery of a rational therapeutic strategy to target the plasticity of melanoma cells associated with resistance. Dedifferentiation is a recurrent innate and acquired resistance mechanism to modern kinase targeted therapies and immunotherapies in the clinic. Thus, ferroptosis-inducing drugs offer a potential up-front co-treatment component, targeted directly at the dedifferentiation-based resistance escape route that limits the efficacy of current lines of melanoma therapy.

Web Resource: Melanoma Gene Expression PCA Maps

To allow users to visualize gene expression trends among the subtypes and within the bulk tumors in PCA space, we have created an interactive Web-interface resource available at <http://systems.crump.ucla.edu/dediff/>.

STAR★METHODS

Detailed methods are provided in the online version of this paper and include the following:

- KEY RESOURCES TABLE
- CONTACT FOR REAGENT AND RESOURCE SHARING
- EXPERIMENTAL MODEL AND SUBJECT DETAILS
- METHOD DETAILS
 - RNA Extraction, Sequencing, and Analysis
 - Clonogenic Survival, Viability and Cytotoxicity Assays
 - Analysis of Reactive Oxygen Species Production
 - Immunoblotting
 - Mass Spectrometry-based Metabolomic Analyses
 - GSH Measurement
- QUANTIFICATION AND STATISTICAL ANALYSIS
 - Classification of Cell Lines and Tumors
 - PCA and Statistical Analysis
 - Enrichment Analysis, Subtype Signatures, and Differentiation Trajectory Scores
 - Immune and Keratin Confounding Signature Criteria
 - Methylation Analysis
- DATA AND SOFTWARE AVAILABILITY
 - Deposited Data
 - Public Data Resources

SUPPLEMENTAL INFORMATION

Supplemental Information includes seven figures and five tables and can be found with this article online at <https://doi.org/10.1016/j.ccell.2018.03.017>.

ACKNOWLEDGMENTS

We thank Heather Christofk and members of our labs for helpful suggestions. This study was funded by the NIH/NCI grants P01 CA168585, R21 CA169993, R35 CA197633, and R01 CA170689, and by the Parker Institute for Cancer Immunotherapy. T.G.G. is supported by an American Cancer Society Research Scholar Award (RSG-12-257-01-TBE), a Melanoma Research Alliance Established Investigator Award (20120279), the UCLA Jonsson Cancer Center Foundation, the National Center for Advancing Translational Sciences UCLA CTSI Grant UL1TR000124, and a Concern Foundation CONquer CanCER Now Award. A.R. is supported by the Dr. Robert Vigen Memorial Fund, the Garcia-Corsini Family Fund, the Ressler Family Fund, and the Grimaldi Family Fund. J.T. is supported by the NIH Ruth L. Kirschstein Institutional National Research Service Award #T32-CA009120. L.R. was supported by the V Foundation-Gil Nickel Family Endowed Fellowship in Melanoma Research and the Spanish Society of Medical Oncology (SEOM) for Translational Research in Reference Centers. K.M.S. is supported by the UCLA Medical Scientist Training Program (NIH NIGMS TG GM08042).

AUTHOR CONTRIBUTIONS

J.T., L.R., A.R., and T.G.G. designed the experiments. J.T. performed the majority of experiments. J.T., K.M.S., and C.S.G. performed bioinformatics analyses. L.R. performed the BRAFi treatment time point studies. L.R., D.J.L.W., and M.A. performed the RNA extraction of the melanoma cell lines. K.P., J.L., and D.B. performed metabolomics. K.P. assisted with cell line characterization. X.W. performed and guided the statistical analysis. K.P. and N.P. provided experimental and analysis input. C.G. and R.S. performed viability assays. J.T., C.S.G., A.R., and T.G.G. wrote the manuscript with input from all authors.

DECLARATION OF INTERESTS

The authors declare that there are no competing interests.

Received: July 6, 2017

Revised: December 1, 2017

Accepted: March 16, 2018

Published: April 12, 2018

REFERENCES

Anders, S., Pyl, P.T., and Huber, W. (2015). HTSeq—a Python framework to work with high-throughput sequencing data. *Bioinformatics* *31*, 166–169.

Caramel, J., Papadogeorgakis, E., Hill, L., Browne, G.J., Richard, G., Wierinckx, A., Saldanha, G., Osborne, J., Hutchinson, P., Tse, G., et al. (2013). A switch in the expression of embryonic EMT-inducers drives the development of malignant melanoma. *Cancer Cell* *24*, 466–480.

Chen, Y., Lemire, M., Choufani, S., Butcher, D.T., Grafodatskaya, D., Zanke, B.W., Gallinger, S., Hudson, T.J., and Weksberg, R. (2013). Discovery of cross-reactive probes and polymorphic CpGs in the Illumina Infinium HumanMethylation450 microarray. *Epigenetics* *8*, 203–209.

Denat, L., Kadekaro, A.L., Marrot, L., Leachman, S.A., and Abdel-Malek, Z.A. (2014). Melanocytes as instigators and victims of oxidative stress. *J. Invest. Dermatol.* *134*, 1512–1518.

Denecker, G., Vandamme, N., Akay, Ö., Koludrovic, D., Taminau, J., Lemeire, K., Gheldof, A., De Craene, B., Van Gele, M., Brochez, L., et al. (2014). Identification of a ZEB2-MITF-ZEB1 transcriptional network that controls melanogenesis and melanoma progression. *Cell Death Differ.* *21*, 1250–1261.

Dixon, S.J., Lemberg, K.M., Lamprecht, M.R., Skouta, R., Zaitsev, E.M., Gleason, C.E., Patel, D.N., Bauer, A.J., Cantley, A.M., Yang, W.S., et al.

(2012). Ferroptosis: an iron-dependent form of nonapoptotic cell death. *Cell* *149*, 1060–1072.

Eroglu, Z., and Ribas, A. (2016). Combination therapy with BRAF and MEK inhibitors for melanoma: latest evidence and place in therapy. *Ther. Adv. Med. Oncol.* *8*, 48–56.

Fallahi-Sichani, M., Becker, V., Izar, B., Baker, G.J., Lin, J.-R., Boswell, S.A., Shah, P., Rotem, A., Garraway, L.A., and Sorger, P.K. (2017). Adaptive resistance of melanoma cells to RAF inhibition via reversible induction of a slowly dividing de-differentiated state. *Mol. Syst. Biol.* *13*, 905.

Hangauer, M.J., Viswanathan, V.S., Ryan, M.J., Bole, D., Eaton, J.K., Matov, A., Galeas, J., Dhruv, H.D., Berens, M.E., Schreiber, S.L., et al. (2017). Drug-tolerant persister cancer cells are vulnerable to GPX4 inhibition. *Nature* *551*, 247–250.

Hansen, K.D., Irizarry, R.A., and Wu, Z. (2012). Removing technical variability in RNA-seq data using conditional quantile normalization. *Biostatistics* *13*, 204–216.

Hoek, K.S., Schlegel, N.C., Brafford, P., Sucker, A., Ugurel, S., Kumar, R., Weber, B.L., Nathanson, K.L., Phillips, D.J., Herlyn, M., et al. (2006). Metastatic potential of melanomas defined by specific gene expression profiles with no BRAF signature. *Pigment Cell Res.* *19*, 290–302.

Hoek, K.S., Schlegel, N.C., Eichhoff, O.M., Widmer, D.S., Praetorius, C., Einarsson, S.O., Valgeirsdottir, S., Bergsteinsdottir, K., Schepsky, A., Dummer, R., et al. (2008). Novel MITF targets identified using a two-step DNA microarray strategy. *Pigment Cell Melanoma Res.* *21*, 665–676.

Hoshida, Y., Brunet, J.-P., Tamayo, P., Golub, T.R., and Mesirov, J.P. (2007). Subclass mapping: identifying common subtypes in independent disease data sets. *PLoS One* *2*, e1195.

Hugo, W., Shi, H., Sun, L., Piva, M., Song, C., Kong, X., Moriceau, G., Hong, A., Dahlman, K.B., Johnson, D.B., et al. (2015). Non-genomic and immune evolution of melanoma acquiring MAPKi resistance. *Cell* *162*, 1271–1285.

Iorio, F., Knijnenburg, T.A., Vis, D.J., Bignell, G.R., Menden, M.P., Schubert, M., Aben, N., Goncalves, E., Barthorpe, S., Lightfoot, H., et al. (2016). A landscape of pharmacogenomic interactions in cancer. *Cell* *166*, 740–754.

Iwai, Y., Ishida, M., Tanaka, Y., Okazaki, T., Honjo, T., and Minato, N. (2002). Involvement of PD-L1 on tumor cells in the escape from host immune system and tumor immunotherapy by PD-L1 blockade. *Proc. Natl. Acad. Sci. USA* *99*, 12293–12297.

Kawakami, Y., Dang, N., Wang, X., Tupesis, J., Robbins, P.F., Wang, R.F., Wunderlich, J.R., Yannelli, J.R., and Rosenberg, S.A. (2000). Recognition of shared melanoma antigens in association with major HLA-A alleles by tumor infiltrating T lymphocytes from 123 patients with melanoma. *J. Immunother.* *23*, 17–27.

Kim, D., Perteau, G., Trapnell, C., Pimentel, H., Kelley, R., and Salzberg, S.L. (2013). TopHat2: accurate alignment of transcriptomes in the presence of insertions, deletions and gene fusions. *Genome Biol.* *14*, R36.

Kim, D., Langmead, B., and Salzberg, S.L. (2015). HISAT: a fast spliced aligner with low memory requirements. *Nat. Methods* *12*, 357–360.

Konieczkowski, D.J., Johannessen, C.M., Abudayyeh, O., Kim, J.W., Cooper, Z.A., Piris, A., Frederick, D.T., Barzily-Rokni, M., Straussman, R., Haq, R., et al. (2014). A melanoma cell state distinction influences sensitivity to MAPK pathway inhibitors. *Cancer Discov.* *4*, 816–827.

Kwong, L.N., Boland, G.M., Frederick, D.T., Helms, T.L., Akid, A.T., Miller, J.P., Jiang, S., Cooper, Z.A., Song, X., Seth, S., et al. (2015). Co-clinical assessment identifies patterns of BRAF inhibitor resistance in melanoma. *J. Clin. Invest.* *125*, 1459–1470.

Landsberg, J., Kohlmeyer, J., Renn, M., Bald, T., Rogava, M., Cron, M., Fatho, M., Lennerz, V., Wölfel, T., Hölzel, M., et al. (2012). Melanomas resist T-cell therapy through inflammation-induced reversible dedifferentiation. *Nature* *490*, 412–416.

Lauss, M., Haq, R., Cirenajwis, H., Phung, B., Harbst, K., Staaf, J., Rosengren, F., Holm, K., Aine, M., Jirstrom, K., et al. (2015). Genome-wide DNA methylation analysis in melanoma reveals the importance of CpG methylation in MITF regulation. *J. Invest. Dermatol.* *135*, 1820–1828.

- Li, F.Z., Dhillon, A.S., Anderson, R.L., McArthur, G., and Ferrao, P.T. (2015). Phenotype switching in melanoma: implications for progression and therapy. *Front. Oncol.* 5, 31.
- Lito, P., Pratilas, C.A., Joseph, E.W., Tadi, M., Halilovic, E., Zubrowski, M., Huang, A., Wong, W.L., Callahan, M.K., Merghoub, T., et al. (2012). Relief of profound feedback inhibition of mitogenic signaling by RAF inhibitors attenuates their activity in BRAFV600E melanomas. *Cancer Cell* 22, 668–682.
- Liu, F., Fu, Y., and Meyskens, F.L., Jr. (2009). MITF regulates cellular response to reactive oxygen species through transcriptional regulation of APE-1/Ref-1. *J. Invest. Dermatol.* 129, 422–431.
- Liu, Y., Hayes, D.N., Nobel, A., and Marron, J.S. (2008). Statistical significance of clustering for high-dimension, low-sample size data. *J. Am. Stat. Assoc.* 103, 1281–1293.
- Luke, J.J., Flaherty, K.T., Ribas, A., and Long, G.V. (2017). Targeted agents and immunotherapies: optimizing outcomes in melanoma. *Nat. Rev. Clin. Oncol.* 14, 463.
- Mica, Y., Lee, G., Chambers, S.M., Tomishima, M.J., and Studer, L. (2013). Modeling neural crest induction, melanocyte specification, and disease-related pigmentation defects in hESCs and patient-specific iPSCs. *Cell Rep.* 3, 1140–1152.
- Moll, R., Divo, M., and Langbein, L. (2008). The human keratins: biology and pathology. *Histochem. Cell Biol.* 129, 705–733.
- Monti, S., Tamayo, P., Mesirov, J., and Golub, T. (2003). Consensus clustering: a resampling-based method for class discovery and visualization of gene expression microarray data. *Mach. Learn.* 52, 91–118.
- Müller, J., Krijgsman, O., Tsoi, J., Robert, L., Hugo, W., Song, C., Kong, X., Possik, P.A., Cornelissen-Steijger, P.D.M., Foppen, M.H.G., et al. (2014). Low MITF/AXL ratio predicts early resistance to multiple targeted drugs in melanoma. *Nat. Commun.* 5, 5712.
- Natarajan, V.T., Ganju, P., Singh, A., Vijayan, V., Kirty, K., Yadav, S., Puntambekar, S., Bajaj, S., Dani, P.P., Kar, H.K., et al. (2014). IFN- γ signaling maintains skin pigmentation homeostasis through regulation of melanosome maturation. *Proc. Natl. Acad. Sci. USA* 111, 2301–2306.
- Nazarian, R., Shi, H., Wang, Q., Kong, X., Koya, R.C., Lee, H., Chen, Z., Lee, M.-K., Attar, N., Sazegar, H., et al. (2010). Melanomas acquire resistance to B-RAF(V600E) inhibition by RTK or N-RAS upregulation. *Nature* 468, 973–977.
- Paraiso, K.H.T., Fedorenko, I.V., Cantini, L.P., Munko, A.C., Hall, M., Sondak, V.K., Messina, J.L., Flaherty, K.T., and Smalley, K.S.M. (2010). Recovery of phospho-ERK activity allows melanoma cells to escape from BRAF inhibitor therapy. *Br. J. Cancer* 102, 1724–1730.
- Piskounova, E., Agathocleous, M., Murphy, M.M., Hu, Z., Huddlestone, S.E., Zhao, Z., Leitch, A.M., Johnson, T.M., DeBerardinis, R.J., and Morrison, S.J. (2015). Oxidative stress inhibits distant metastasis by human melanoma cells. *Nature* 527, 186–191.
- Poole, W., Gibbs, D.L., Shmulevich, I., Bernard, B., and Knijnenburg, T.A. (2016). Combining dependent P-values with an empirical adaptation of Brown's method. *Bioinformatics* 32, i430–i436.
- Poulikakos, P.I., Persaud, Y., Janakiraman, M., Kong, X., Ng, C., Moriceau, G., Shi, H., Atefi, M., Titz, B., Gabay, M.T., et al. (2011). RAF inhibitor resistance is mediated by dimerization of aberrantly spliced BRAF(V600E). *Nature* 480, 387–390.
- Raj, L., Ide, T., Gurkar, A.U., Foley, M., Schenone, M., Li, X., Tolliday, N.J., Golub, T.R., Carr, S.A., Shamji, A.F., et al. (2011). Selective killing of cancer cells by a small molecule targeting the stress response to ROS. *Nature* 475, 231–234.
- Ramirez, M., Rajaram, S., Steininger, R.J., Osipchuk, D., Roth, M.A., Morinishi, L.S., Evans, L., Ji, W., Hsu, C.-H., Thurlley, K., et al. (2016). Diverse drug-resistance mechanisms can emerge from drug-tolerant cancer persister cells. *Nat. Commun.* 7, 10690.
- Riesenberg, S., Groetchen, A., Siddaway, R., Bald, T., Reinhardt, J., Smorra, D., Kohlmeyer, J., Renn, M., Phung, B., Aymans, P., et al. (2015). MITF and c-Jun antagonism interconnects melanoma dedifferentiation with pro-inflammatory cytokine responsiveness and myeloid cell recruitment. *Nat. Commun.* 6, 8755.
- Rodeck, U., Nishiyama, T., and Mauviel, A. (1999). Independent regulation of growth and SMAD-mediated transcription by transforming growth factor β in human melanoma cells. *Cancer Res.* 59, 547–550.
- Sauka-Spengler, T., and Bronner-Fraser, M. (2008). A gene regulatory network orchestrates neural crest formation. *Nat. Rev. Mol. Cell Biol.* 9, 557–568.
- Schepsky, A., Bruser, K., Gunnarsson, G.J., Goodall, J., Hallsson, J.H., Goding, C.R., Steingrímsson, E., and Hecht, A. (2006). The microphthalmia-associated transcription factor Mitf interacts with β -catenin to determine target gene expression. *Mol. Cell. Biol.* 26, 8914–8927.
- Seashore-Ludlow, B., Rees, M.G., Cheah, J.H., Cokol, M., Price, E.V., Coletti, M.E., Jones, V., Bodycombe, N.E., Soule, C.K., Gould, J., et al. (2015). Harnessing connectivity in a large-scale small-molecule sensitivity dataset. *Cancer Discov.* 5, 1210–1223.
- Shaffer, S.M., Dunagin, M.C., Torborg, S.R., Torre, E.A., Emert, B., Krepler, C., Beqiri, M., Sproesser, K., Brafford, P.A., Xiao, M., et al. (2017). Rare cell variability and drug-induced reprogramming as a mode of cancer drug resistance. *Nature* 546, 431.
- Shakhova, O., Zingg, D., Schaefer, S.M., Hari, L., Civenni, G., Blunski, J., Claudinot, S., Okoniewski, M., Beermann, F., Mihic-Probst, D., et al. (2012). Sox10 promotes the formation and maintenance of giant congenital naevi and melanoma. *Nat. Cell Biol.* 14, 882–890.
- Shi, P., Ray, S., Zhu, Q., and Kon, M.A. (2011). Top scoring pairs for feature selection in machine learning and applications to cancer outcome prediction. *BMC Bioinformatics* 12, 375.
- Søndergaard, J.N., Nazarian, R., Wang, Q., Guo, D., Hsueh, T., Mok, S., Sazegar, H., MacConaill, L.E., Baretina, J.G., Kehoe, S.M., et al. (2010). Differential sensitivity of melanoma cell lines with BRAF V600E mutation to the specific Raf inhibitor PLX4032. *J. Transl. Med.* 8, 39.
- Soudja, S.M., Wehbe, M., Mas, A., Chasson, L., de Tenbossche, C.P., Huijbers, I., Van den Eynde, B.V., and Schmitt-Verhulst, A.M. (2010). Tumor-initiated inflammation overrides protective adaptive immunity in an induced melanoma model in Mice. *Cancer Res.* 70, 3515–3525.
- Spitz, F., and Furlong, E.E.M. (2012). Transcription factors: from enhancer binding to developmental control. *Nat. Rev. Genet.* 13, 613–626.
- Sun, C., Wang, L., Huang, S., Heynen, G.J.J.E., Prahallad, A., Robert, C., Haanen, J., Blank, C., Wesseling, J., Willems, S.M., et al. (2014). Reversible and adaptive resistance to BRAF(V600E) inhibition in melanoma. *Nature* 508, 118–122.
- Taube, J.M., Anders, R.A., Young, G.D., Xu, H., Sharma, R., McMiller, T.L., Chen, S., Klein, A.P., Pardoll, D.M., Topalian, S.L., et al. (2012). Colocalization of inflammatory response with B7-H1 expression in human melanocytic lesions supports an adaptive resistance mechanism of immune escape. *Sci. Transl. Med.* 4, 127ra37.
- Telley, L., Govindan, S., Prados, J., Stevant, I., Nef, S., Dermitzakis, E., Dayer, A., and Jabaudon, D. (2016). Sequential transcriptional waves direct the differentiation of newborn neurons in the mouse neocortex. *Science* 351, 1443–1446.
- Tirosh, I., Izar, B., Prakadan, S.M., Wadsworth, M.H., Treacy, D., Trombetta, J.J., Rotem, A., Rodman, C., Lian, C., Murphy, G., et al. (2016). Dissecting the multicellular ecosystem of metastatic melanoma by single-cell RNA-seq. *Science* 352, 189–196.
- Titz, B., Lomova, A., Le, A., Hugo, W., Kong, X., ten Hoeve, J., Friedman, M., Shi, H., Moriceau, G., Song, C., et al. (2016). JUN dependency in distinct early and late BRAF inhibition adaptation states of melanoma. *Cell Discov.* 2, 16028.
- Trapnell, C., Roberts, A., Goff, L., Pertea, G., Kim, D., Kelley, D.R., Pimentel, H., Salzberg, S.L., Rinn, J.L., and Pachter, L. (2012). Differential gene and transcript expression analysis of RNA-seq experiments with TopHat and Cufflinks. *Nat. Protoc.* 7, 562–578.
- Tusher, V.G., Tibshirani, R., and Chu, G. (2001). Significance analysis of microarrays applied to the ionizing radiation response. *Proc. Natl. Acad. Sci. USA* 98, 5116–5121.
- Vazquez, F., Lim, J.-H., Chim, H., Bhalla, K., Gimun, G., Pierce, K., Clish, C.B., Granter, S.R., Widlund, H.R., Spiegelman, B.M., et al. (2013). PGC1 α expression defines a subset of human melanoma tumors with increased

mitochondrial capacity and resistance to oxidative stress. *Cancer Cell* 23, 287–301.

Viswanathan, V.S., Ryan, M.J., Dhruv, H.D., Gill, S., Eichhoff, O.M., Seashore-Ludlow, B., Kaffenberger, S.D., Eaton, J.K., Shimada, K., Aguirre, A.J., et al. (2017). Dependency of a therapy-resistant state of cancer cells on a lipid peroxidase pathway. *Nature* 547, 453–457.

Wilkerson, M.D., and Hayes, D.N. (2010). ConsensusClusterPlus: a class discovery tool with confidence assessments and item tracking. *Bioinformatics* 26, 1572–1573.

Yagoda, N., von Rechenberg, M., Zaganjor, E., Bauer, A.J., Yang, W.S., Fridman, D.J., Wolpaw, A.J., Smukste, I., Peltier, J.M., Boniface, J.J., et al.

(2007). RAS–RAF–MEK-dependent oxidative cell death involving voltage-dependent anion channels. *Nature* 447, 865–869.

Yang, W.S., and Stockwell, B.R. (2008). Synthetic lethal screening identifies compounds activating iron-dependent, nonapoptotic cell death in oncogenic-RAS-harboring cancer cells. *Chem. Biol.* 15, 234–245.

Yang, W.S., SriRamaratnam, R., Welsch, M.E., Shimada, K., Skouta, R., Viswanathan, V.S., Cheah, J.H., Clemons, P.A., Shamji, A.F., Clish, C.B., et al. (2014). Regulation of ferroptotic cancer cell death by GPX4. *Cell* 156, 317–331.

Yang, W.S., Kim, K.J., Gaschler, M.M., Patel, M., Shchepinov, M.S., and Stockwell, B.R. (2016). Peroxidation of polyunsaturated fatty acids by lipoxygenases drives ferroptosis. *Proc. Natl. Acad. Sci. USA* 113, E4966–E4975.

STAR★METHODS

KEY RESOURCES TABLE

REAGENT or RESOURCE	SOURCE	IDENTIFIER
Antibodies		
Anti-AXL (C89E7)	Cell Signaling	Cat#8661; RRID: AB_11217435
Anti-MITF (D5G7V)	Cell Signaling	Cat#12590; RRID: AB_2616024
Anti-p75NTR (D4B3) XP® Rabbit mAb	Cell Signaling	Cat#8238; RRID: AB_10839265
Anti-MART-1 (A103)	Santa Cruz	Cat#sc-20032; RRID: AB_2713930
Anti-β-Actin (AC-15)	Sigma-Aldrich	Cat#A1978; RRID: AB_476692
Anti-p44/42 MAPK (Erk1/2) (L34F12)	Cell Signaling	Cat#4696; RRID: AB_390780
Anti-phospho-p44/42 MAPK (Erk1/2) (Thr202/Tyr204) (D13.14.4E)	Cell Signaling	Cat#4370; RRID: AB_2315112
Anti-STAT1	Cell Signaling	Cat#9172; RRID: AB_2198300
Anti-pSTAT1 (Y701) (58D6)	Cell Signaling	Cat#9167; RRID: AB_561284
Anti-NF-κB p65 (D14E12) XP® Rabbit mAb	Cell Signaling	Cat#8242; RRID: AB_10859369
Anti-Phospho-NF-κB p65 (Ser536) (93H1)	Cell Signaling	Cat#3033; RRID: AB_331284
IRDye 800CW Goat Anti-Mouse IgG	LI-COR	Cat#926-32210; RRID: AB_621842
IRDye 680 Goat Anti-Rabbit IgG	LI-COR	Cat#926-32221; RRID: AB_621841
Chemicals, Peptides, and Recombinant Proteins		
Vemurafenib (PLX 4032)	Selleck Chemicals	S1267; CAS: 918504-65-1
Erastin	Selleck Chemicals	S7242; CAS: 571203-78-6
RSL3	Selleck Chemicals	S8155; CAS: 1219810-16-8
Z-VAD-FMK	Selleck Chemicals	S7023; CAS: 187389-52-2
L-Glutathione reduced	Sigma-Aldrich	G4251; CAS: 70-18-8
Piperlongumine	Selleck Chemicals	S7551; CAS: 20069-09-4
Deferoxamine	Sigma-Aldrich	D9533; CAS: 138-14-7
Resazurin	Sigma-Aldrich	R7017; CAS: 62758-13-8
Trolox	Acros Organics	Cat#218940010; CAS: 53188-07-1
Staurosporine	Cayman Chemicals	S1421; CAS: 62996-74-1
Recombinant Human TNF α	Peprtech	Cat#300-01A
Recombinant Human IFN γ	Peprtech	Cat#300-02
Critical Commercial Assays		
QuantiChrom Glutathione (GSH) Assay Kit	BioAssay Systems	DIGT-250
Cell-Titer Glo	Promega	G7572
GenePrint® 10 System	Promega	B9510
AllPrep DNA/RNA Mini kit	Qiagen	Cat#80204
Illumina TruSeq RNA sample preparation kit	Illumina	RS-122-2001
TruPAGE™ Precast Gels 4-12%,	Sigma-Aldrich	PCG2003
Pierce BCA Protein Assay Kit	Thermo Scientific	Cat#23225
CM-H2DCFDA	Life Technologies	C6827

(Continued on next page)

Continued

REAGENT or RESOURCE	SOURCE	IDENTIFIER
BODIPY 581/591 C11	Life Technologies	D3861
Trypan Blue	Gibco	15250061
IncuCyte Cytotox Red Reagent	Essen Bioscience	Cat#4632
Deposited Data		
RNASeq of melanoma cell lines	GSE80829	N/A
RNASeq of vemurafenib treatment timecourse	GSE110054	N/A
Experimental Models: Cell Lines		
Human: M-series patient derived cell lines	This paper; Drs. James Economou, Antoni Ribas, and Roger Lo Labs	Søndergaard et al., 2010
Software and Algorithms		
GraphPad Prism 6	GraphPad	N/A
TraceFinder Software version 3.3	Thermo Scientific	N/A
ImageStudioLite	LI-COR	www.licor.com/bio/products/software/image_studio_lite/
IncuCyte ZOOM Live-Cell Imaging System	Essen Bioscience	N/A
HISAT2 (v.2.0.5)	(Kim et al., 2015)	https://ccb.jhu.edu/software/hisat2/index.shtml
HTSeq (0.6.1)	(Anders et al., 2015)	https://ccb.jhu.edu/software/hisat2/index.shtml
Tophat2 (v2.0.9)	(Kim et al., 2013)	https://ccb.jhu.edu/software/tophat/
Cufflinks (v2.2.1)	(Trapnell et al., 2012)	http://cole-trapnell-lab.github.io/cufflinks/
Gene Set Enrichment Analysis (GSEA)	N/A	http://software.broadinstitute.org/gsea/index.jsp
R (v3.2)	N/A	https://www.r-project.org/
ConsensusClusterPlus R Bioconductor Package (v1.38)	(Wilkerson and Hayes, 2010)	http://bioconductor.org/packages/release/bioc/html/ConsensusClusterPlus.html
Conditional Quantile Normalization R Bioconductor Package (v1.20)	(Hansen et al., 2012)	https://bioconductor.org/packages/release/bioc/html/cqn.html
sigclust R Package (v1.1)	(Liu et al., 2008)	https://cran.r-project.org/web/packages/sigclust/index.html
samr R Package (v2.0)	(Tusher et al., 2001)	https://cran.r-project.org/web/packages/samr/index.html
metap	N/A	https://cran.r-project.org/web/packages/metap/index.html
EmpiricalBrownsMethod	(Poole et al., 2016)	http://bioconductor.org/packages/release/bioc/html/EmpiricalBrownsMethod.html
clinfun	N/A	https://cran.r-project.org/web/packages/clinfun/index.html
FSA	N/A	https://cran.r-project.org/web/packages/FSA/index.html

CONTACT FOR REAGENT AND RESOURCE SHARING

Further information and requests for resources and reagents should be directed to and will be fulfilled by the Lead Contact, Thomas G. Graeber (TGraeber@mednet.ucla.edu).

EXPERIMENTAL MODEL AND SUBJECT DETAILS

Human melanoma cell lines were established from patient's biopsies with informed consent from all subjects under UCLA institutional review board approval # 11-003254. A complete list of cell lines can be found in [Table S1](#). Cells were cultured in RPMI 1640 with L-glutamine, 10% fetal bovine serum, and 1% penicillin, streptomycin and fungizone in a water-saturated incubator at 37°C with 5% CO₂. Cells were maintained and tested for mycoplasma and authenticated to their early passages using GenePrint® 10 System (Promega).

METHOD DETAILS

RNA Extraction, Sequencing, and Analysis

RNA extraction was performed using AllPrep DNA/RNA Mini kit from Qiagen in 53 human melanoma cell lines. Libraries were prepared using the Illumina TruSeq RNA sample preparation kit per the manufacturer's instructions. RNA sequencing was performed

using 50 bp paired end sequencing on the Illumina HiSeq 2000 platform. Paired end 50 bp reads generated from the melanoma cell line RNA sequencing were mapped using HISAT2 to the Homo sapiens hg38 genome build and raw counts were quantified using HTSeq. Both the 53 melanoma cell line panel and TCGA raw expected counts were analyzed similarly to reduce technical variability from data processing. Cell line and TCGA raw counts were normalized to FPKM values using conditional quantile normalization (CQN) to adjust for gene length and GC content (Hansen et al., 2012). FPKM values were next transformed in log₂ space with an offset of 1. For the vemurafenib treated samples, RNASeq was performed using 50 bp single end sequencing and mapped the Homo sapiens NCBI build 37.2 reference genome using TopHat2 v2.0.9 (Kim et al., 2013) and normalized to fragments per kilobase of exon per million fragments mapped (FPKM) using Cufflinks v2.2.1 and the geometric library size normalization method (Trapnell et al., 2012).

Clonogenic Survival, Viability and Cytotoxicity Assays

For the BRAFi timecourse study, M229 was treated with vemurafenib or DMSO for the indicated timepoints at twice the 50% inhibition concentration (500 nM). For the crystal violet assays, 2.5×10^5 cells were plated in 6-well plates. The next day media was replaced by drug media and replenished every 2-3 days. Plates were stained with crystal violet solution (1% crystal violet, 50% methanol). Control wells were grown for 1 week and stained when 100% confluent. For quantification, crystal violet in the wells were solubilized in 10% acetic acid and absorbance was measured at 570 nm. To combine experiments, linear regression was performed to normalize each experiment to the first. Relative amounts were then normalized to the average DMSO control treatment.

For measurement of percent viable cells with treatment, cells were plated at 5000 cells per well and the next day treated with drug. Percentage cell viability is reported as a percentage relative to the negative control treatment. Dose-response curves were assayed using the ATP-based CellTiter-Glo (Promega) luminescent cell viability assay. IC₅₀ values were obtained by fitting the data to nonlinear regression with variable slope using GraphPad Prism. For other viability measurements, an resazurin-based assay (a.k.a. Alamar Blue) was used and fluorescence was measured at 570/600 ex/em wavelength. Measurement of dead cells per time was measured by incubating treated cells with the IncuCyte Cytotox Red Reagent and imaging with IncuCyte ZOOM Live-Cell Imaging System (Essen BioScience). For measurement of cell death, Trypan blue exclusion assay was used.

Analysis of Reactive Oxygen Species Production

In 12-well plates, 100,000 cells per well were seeded and allowed to attach for approximately 12 hours. Cells were then treated with media containing 5 μM of erastin, 100 μM deferoxamine or a combination of both, and returned to the 37°C tissue culture incubator. After 10 hours, drug media was replaced by media containing DMSO control, 5 μM of CM-H2DCFDA dye (Life Technologies, C6827), or 5 μM of C11-BODIPY (Life Technologies, D3861) and incubated for another 20 min at 37°C. Cells were then washed with PBS, harvested by trypsinization, followed by another wash with PBS. Cells were resuspended in 400 μL PBS, strained through a 35 μm nylon mesh filter, and analyzed by flow cytometry using BD LSRII equipped with 488 nm laser for excitation (BD Biosciences).

Immunoblotting

Cells were lysed in modified RIPA buffer (50 mM Tris-HCl (pH 7.5), 150 NaCl, 10 mM β-glycerophosphate, 1% NP-40, 0.25% sodium deoxycholate, 10 mM sodium pyrophosphate, 30 mM sodium fluoride, 1 mM EDTA, 1 mM vanadate, 20 μg/ml aprotinin, 20 μg/ml leupeptin, and 1 mM phenylmethylsulfonyl fluoride). Whole-cell lysates were resolved by SDS-PAGE on TruPAGE 4–15% gradient gels (Sigma-Aldrich) and blotted onto nitrocellulose membranes. Membranes were blocked overnight with 5% milk and then incubated sequentially with primary and then IRDye-conjugated secondary antibodies (Li-Cor). Blots were imaged using the Odyssey Infrared Imaging System (Li-Cor).

Mass Spectrometry-based Metabolomic Analyses

In 6-well plates, 200,000 cells per seeded per well and allowed to attach over night. The next day, media was replaced with media containing 5 μM of erastin. After 8 hr of treatment, cells were washed with ice-cold 150 mM ammonium acetate (NH₄AcO) pH 7.3 and metabolites extracted in 1 ml ice-cold 80% MeOH. The cells were quickly transferred into a microfuge tube, and 10 nmol norvaline was added to the cell suspension for use as an internal standard. The suspension was subsequently vortexed three times over 15 min and then spun down at 4°C for 5 min. The supernatant was transferred into a glass vial, the cell pellet was re-extracted with 200 μl ice-cold 80% MeOH and spun down and the supernatants were combined. Metabolites were dried at 30°C under vacuum and re-suspended in 50 μl of 70% acetonitrile (ACN).

Samples were run on a Q-Exactive mass spectrometer coupled to an UltiMate 3000RSLC UHPLC system (Thermo Scientific). The mass spectrometer was run in polarity switching mode (+3.00 kV/–2.25 kV) with an m/z window ranging from 65 to 975. Mobile phase A was 5 mM NH₄AcO, pH 9.9, and mobile phase B was ACN. Metabolites were separated on a Luna 3 μm NH₂ 100 Å (150 × 2.0 mm) (Phenomenex) column. The flow was kept at 200 μl/min, and the gradient was from 15% A to 95% A in 18 min, followed by an isocratic step for 9 min and re-equilibration for 7 min. Metabolites were detected and quantified as area under the curve (AUC) based on retention time and accurate mass (≤ 3 ppm) using the TraceFinder 3.1 (Thermo Scientific) software. Samples were normalized by protein concentration measured using the BCA Protein Assay Kit from Pierce Biotechnology. All samples were run as biological triplicates, and consistent results were seen in independent experiments.

GSH Measurement

Levels of GSH were measured using the colorimetric QuantiChrom Glutathione Assay Kit (BioAssay Systems) according to the kit instructions. Briefly, 2×10^6 cells were plated on 10 cm dishes. The next day, cells were scraped with cold PBS and centrifuged at 1000g for 10 minutes at 4°C. Cells were re-suspended in 1 mL cold phosphate buffer (50mM phosphate, 1 mM EDTA, pH=6.5) and lysed by sonication. Lysates were spun down at 10,000g for 15 min at 4°C. The supernatant was split into two for measurement of GSH using the kit reagents, and protein quantification using the BCA Protein Assay Kit from Pierce Biotechnology.

QUANTIFICATION AND STATISTICAL ANALYSIS

Classification of Cell Lines and Tumors

The top 3000 genes with the highest variance were used for clustering. Consensus complete linkage hierarchical clustering was performed using the Euclidean distance metric and subsampling 75% of samples and genes 1000 times using the *ConsensusClusterPlus* R package. Pairwise cluster significance, as defined by whether each cluster originates from different Gaussian distributions, was performed using the *sigclust* R package. A support vector machine (SVM) “top-scoring pairs” (TSP)-based approach, designed for cross-platform/cross-batch application (Shi et al., 2011), was used to train the subtype prediction model. To have a gene list compatible for all datasets used, we took an intersection of genes from both RNASeq and microarray chip platforms, resulting in 10,545 genes. The top 250 genes with highest variance in the training set were used to build the model. The gene expression matrix was converted into a gene pair binary matrix of relative comparisons for each pair of genes A and B whether A>B based on the top-scoring pairs approach. Pairs were then scored by hypergeometric test to calculate the p value of enrichment for each subtype compared to the remaining subtypes. Gene-pairs were filtered by a minimum p value of $1e-05$ in at least one subtype, resulting in 1561 gene-pairs. The resulting binary matrix of each cell line with identified subtype was used to train the model using a radial basis function kernel with the R package *kernelab*. The model performed at 94% accuracy with leave-one-out cross validation. Gene expression profiles for all prediction datasets were similarly converted to binary matrices and used as test sets for the SVM-based predictions.

PCA and Statistical Analysis

Principal component analysis (PCA) was performed on mean centered data and statistical analyses were performed in R (<http://www.R-project.org/>). Projections were calculated by matrix multiplication of the centered data to be projected and the rotation matrix determined from the PCA of the original source data.

Significance testing between treatment groups was performed using two-tailed two-sample t-test unless otherwise indicated. Multi-group ANOVA p values were determined using the non-parametric Kruskal-Wallis test at a significance threshold of 0.05. Reported p values between pairs of subtypes were determined using Dunn post-hoc testing with multiple hypothesis correction using the Benjamini & Hochberg method through the R “FSA” package. The combined p value for the trend of increased ferroptosis sensitivity with dedifferentiation across both the CTRP results and the validation results is based on correlation ($p=10^{-12}$) with similar results with Jonckheere-Terpstra trend test assessing ordered significance across the 4 differentiation stages ($p=10^{-13}$). In the overall analysis of IC_{50} sensitivity versus differentiation state, we combined p values by first adapting Brown’s method, a more conservative extension of Fisher’s method, to account for reduced independence of testing the same cell lines using different inhibitors (Poole et al., 2016). Then Fisher’s method was applied to combine the p values from the independent CRTP and UCLA data. These analyses were conducted using R packages “EmpiricalBrownsMethod” and “metap.” The Jonckheere–Terpstra test was performed with the R “clinfun” package.

Enrichment Analysis, Subtype Signatures, and Differentiation Trajectory Scores

For subtype comparisons, signal-to-noise ratio of one subtype vs. the remaining three were used to create ranklists. Enrichment analysis was performed using Gene Set Enrichment Analysis (GSEA) using the MSigDB C5 GO biological process gene sets. Differential expression analysis used for generating subtype signatures was performed using Significance Analysis of Microarrays with a log2 fold change threshold of 1.5 and 5% false discovery rate (FDR) using the “samr” package in R. For average subtype signature scores, z-scores for all member genes were summed and divided by the number of member genes. To avoid potential confounding issues with gene expression from non-tumor sources, genes correlated with the immune and keratin signature were not included. Differentiation trajectory position score was determined using a center of mass approach where all single subtype and transitional-paired subtype average signature scores were summed in a weighted fashion. Weighting represented the relative position along the differentiation trajectory (i) running from 1 to 7 for undifferentiated, undifferentiated-neural crest pair, neural crest, neural crest-transitory pair, transitory, transitory-melanocytic pair, and melanocytic. The formula is given by:

$$\text{Differentiation Trajectory Position} = \frac{\sum_{i=1}^7 m_i \cdot i}{\sum_{i=1}^7 m_i}$$

where m_i are the seven signature scores.

Immune and Keratin Confounding Signature Criteria

A starter list of immune genes was obtained from the Immune database, downloaded from InnateDB (<http://www.innatedb.com>). PCA was used to reduce dimensionality of the list of immune genes to a single immune score (PC1). The total list of immune confounded genes was determined by identifying genes that were correlated to the immune score above a threshold value. The threshold correlation was determined using an ROC analysis, comparing distributions of correlations of genes within the immune starter list vs. all others. Keratin confounded genes was identified similarly, using genes annotated as keratins from the NCBI gene database (<http://www.ncbi.nlm.nih.gov/gene/>) as the starter list of genes.

Methylation Analysis

Human tumor methylation 450K array data was obtained from The Cancer Genome Atlas. Cell line methylation 450K array data was obtained from GSE68379. Probes excluded from the downstream analysis were probes with poor detection quality, probes mapping to sex chromosomes, probes with known SNPs at the CG site, and 29,233 probes previously shown to be cross-reactive with genes on sex chromosomes (Chen et al., 2013). Using the UCSC gene annotation, probes mapping to the promoter (TSS1500, TSS200, 5'UTR, and 1stExon) were collapsed to gene level by averaging the sites mapping to each gene. Probes mapping to CG islands and probes mapping to multiple genes were excluded, resulting in gene-level promoter methylation values for 15,580 genes for the cell line data and 14,318 genes for the TCGA data.

DATA AND SOFTWARE AVAILABILITY

Deposited Data

The data reported in this paper is deposited in the Gene Expression Omnibus (GEO) database under accession numbers GSE80829 and GSE110054.

Public Data Resources

Dataset from Mica *et al* for the melanocyte differentiation stage analysis was obtained from GSE45227. Gene expression profiles from samples representing the growth conditions for each specified stage of differentiation based on the original manuscript was used for analysis (day 0 embryonic stem cell, day 6 neural crest cell, day 11 melanoblast, and day 25 melanocyte). Primary melanocyte expression profiles (adult and neonatal) were used as control.

Data from the CCLE (expression) and GDSC (expression and methylation) databases were downloaded from the respective resource websites (<http://www.broadinstitute.org/ccle>; <http://www.cancerxgene.org/downloads>). For expression analysis, microarray probes were collapsed to gene symbol to the maximum average probe. Pharmacogenomic data from the CTRP was downloaded from the Cancer Target Discovery and Development (CTD²) data portal (<https://ocg.cancer.gov/programs/ctd2/data-portal>). For subtype annotations of cell lines used in the pharmacogenomics analysis, we used our support vector machine (SVM)-based classifier and merged both the CCLE and GDSC predictions. Within the 29 cell lines shared between these two datasets, 27 were identically predicted (93.1%) and the other two only shifted by 1 stepwise differentiation state. We excluded 6 cell lines that either had mismatched or non-confident classifications, resulting in 43 lines analyzed (1 assayed in duplicate by the CTRP). While our results show concordance between erastin and GPX4 inhibitors, erastin was somewhat less concordant in the CTRP pharmacogenomics dataset. Among other possibilities, this could be due to the use of different media formulations in the CTRP experiments, which can impact redox metabolism and the degree of GSH depletion achieved by erastin.

For the data from Landsberg *et al*, expression profiles were obtained from GSE40213. Mouse genes were mapped to human homologs using the NCBI HomoloGene database. To account for any genes that might not vary in a mouse and could dilute signal when switching to human analysis, a variance filter of 0.3 was applied.

RNASeq raw expected counts (RNASeqV2) and DNA methylation beta values (HM450K) of skin cutaneous melanoma (SKCM) bulk tumors from The Cancer Genome Atlas (TCGA) were downloaded from the data portal (<http://tcga-data.nci.nih.gov>). For MAPKi treated data, RSEM TPM expression values of patient tumor samples on-treatment from Kwong *et al* were obtained from European Genome-phenome Archive (EGA S00001000992). FPKM values for single and double drug MAPKi resistant cell lines and disease progression tumors from Hugo *et al* were obtained from GSE65186. FPKM values of disease progression tumors from Tirosh *et al* were obtained from GSE77940.

Cancer Cell, Volume 33

Supplemental Information

Multi-stage Differentiation Defines Melanoma

Subtypes with Differential Vulnerability

to Drug-Induced Iron-Dependent Oxidative Stress

Jennifer Tsoi, Lidia Robert, Kim Paraiso, Carlos Galvan, Katherine M. Sheu, Johnson Lay, Deborah J.L. Wong, Mohammad Atefi, Roksana Shirazi, Xiaoyan Wang, Daniel Braas, Catherine S. Grasso, Nicolaos Palaskas, Antoni Ribas, and Thomas G. Graeber

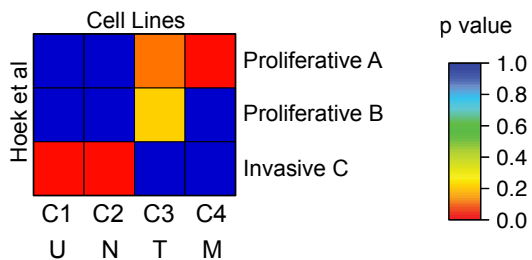
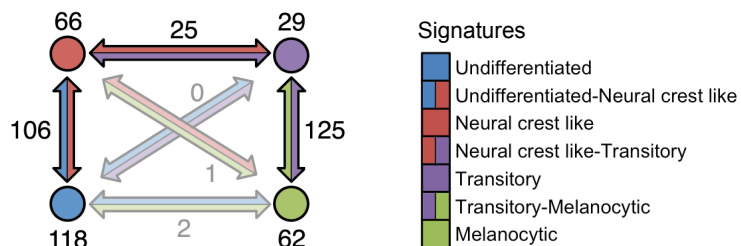
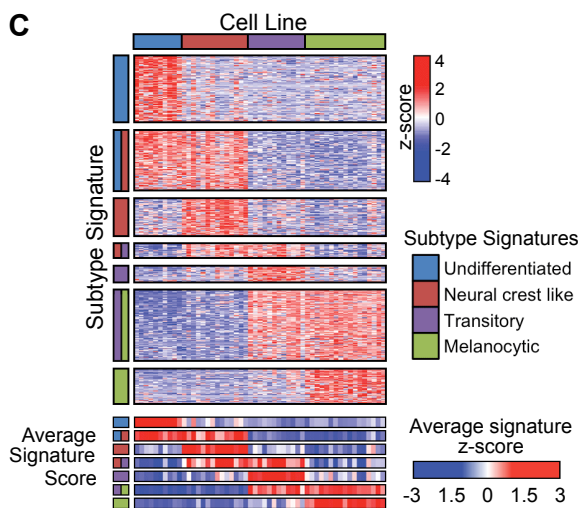
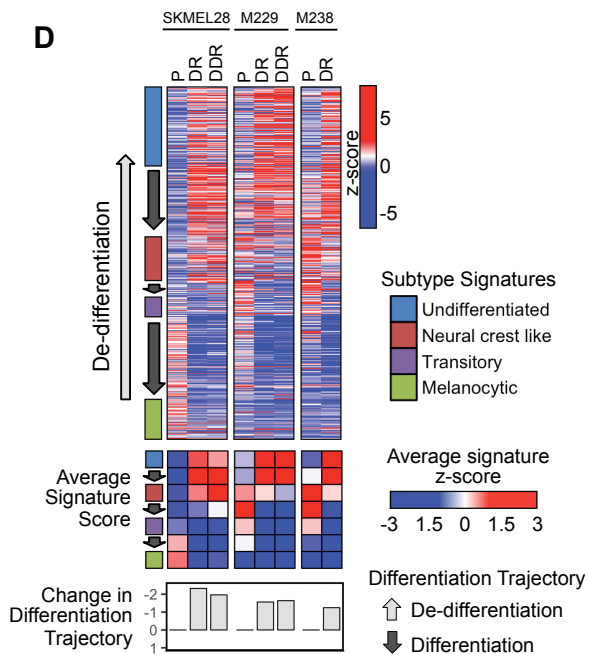
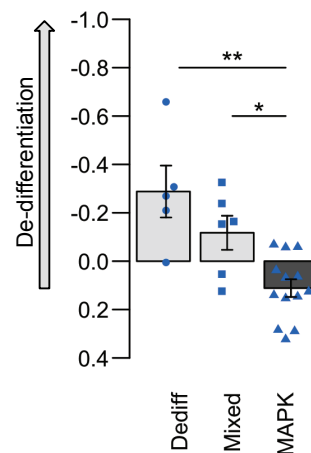
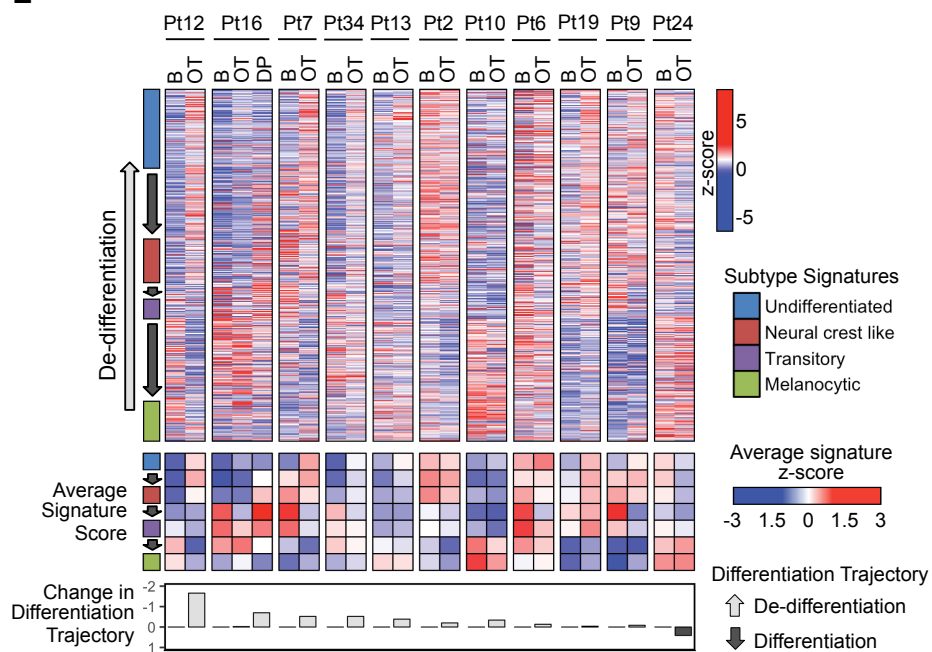
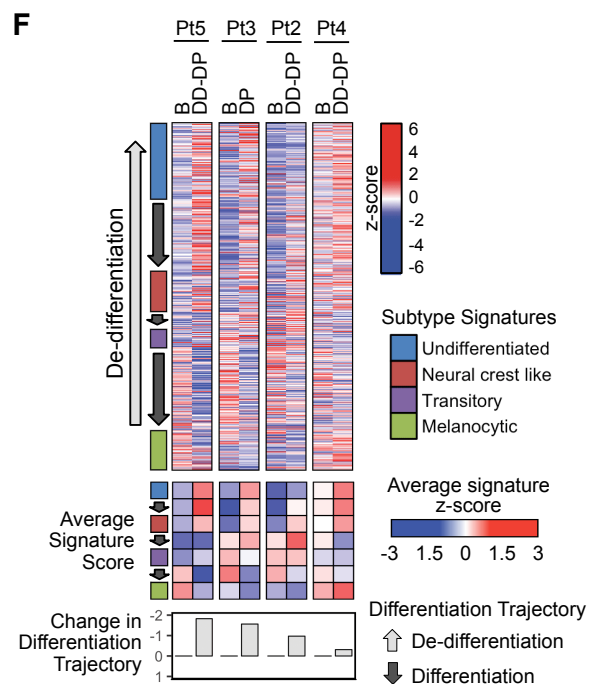
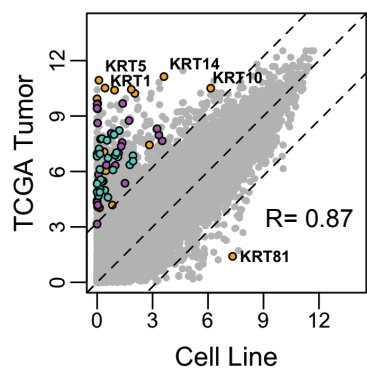
A**B****C****D****G****E****F**

Figure S1. Identification of subtype signatures for scoring and visualization of treatment-induced dedifferentiation. Related to Figure 2.

(A) SubMap analysis showing mapping between the Hoek invasive-proliferative classification and our four-group classification. (B) Numbers of differentially upregulated genes in each individual subtype or shared between pairs of subtypes when compared to the remaining subtypes (\log_2 fold change ≥ 1.5 , 5% false discovery rate). (C) Heatmap of subtype gene signatures in cell line gene expression profiles. Average of each subtype signature z-score are shown at the bottom. (D) Heatmap of signature genes, average signature z-scores, and differentiation trajectory position changes for matched parental (P) or single drug resistant (DR) or double drug resistant (DDR) samples of the three indicated cell lines. Single drug: vemurafenib (BRAFi); double drug: vemurafenib + selumetinib (MEKi). (E) Heatmap of signature genes, average signature z-scores, and differentiation trajectory position changes at baseline, on-treatment or disease progression for 11 melanoma patient (Pt) treatment cases (B: baseline, OT: on-treatment, DP: disease progression). All patients were on double drug (dabrafenib + trametinib (BRAFi+MEKi)) therapy with the exception of Pt2 on single drug therapy (vemurafenib (BRAFi)). On treatment samples are 12 ± 5 days (Kwong et al., 2015). (F) Heatmap of subtype signature genes, average subtype signature scores and differentiation trajectory position changes of the 4 reported post-relapse tumors at baseline with statistically significant dedifferentiation at disease progression on double drug therapy (B: baseline, DP: disease progression, DD-DP: double drug disease progression on dabrafenib and trametinib) (of 6 tested) (Tirosh et al., 2016). (G) Barplot of changes in differentiation trajectory score of patient tumors with dedifferentiation, MAPK reactivation, or mixed dedifferentiation and MAPK reactivation markers upon disease progression on therapeutic RAF and/or MEK inhibition (Hugo et al., 2015). Dedifferentiation was determined by MITF downregulation or PDGFRB upregulation as previously observed (Müller et al., 2014). Data shown represents mean \pm sem. MAPK reactivation was determined by upregulation, amplification or alternative splicing of BRAF, or upregulation or mutation of NRAS (Corcoran et al., 2010; Nazarian et al., 2010; Poulikakos et al., 2011). Mixed / heterogeneous response cases had biomarkers for both mechanisms. Pairwise two-tailed p values: * ≤ 0.05 , ** ≤ 0.01 , overall Kruskal-Wallis p value 0.002. For all panels, negative differentiation trajectory position changes reflect dedifferentiation.

A

- Immune CD markers
- Immune Response
- Keratins

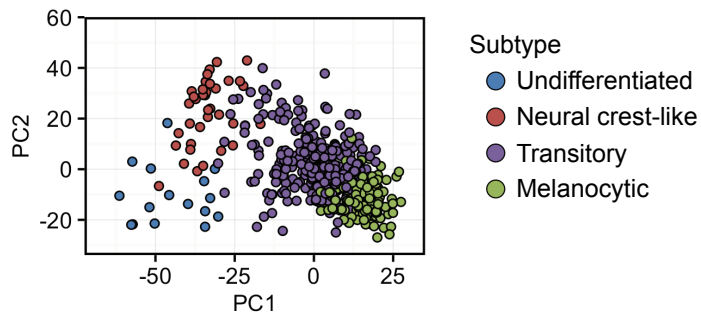
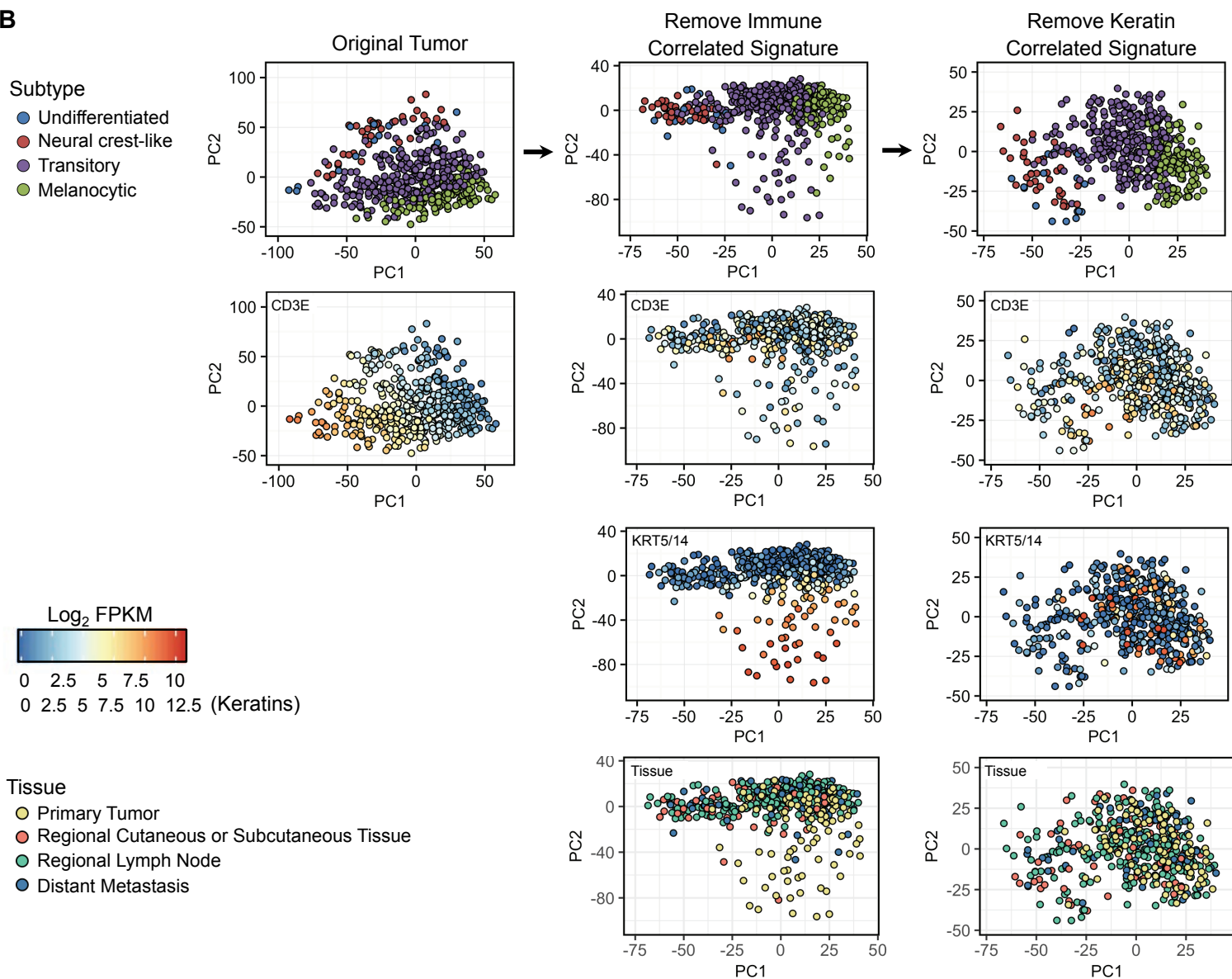
C**B**

Figure S2. Removal of confounding signatures from bulk tumors yields similar PCA results as cell line analysis. Related to Figure 3.

(A) Scatterplot of maximum gene expression in the melanoma bulk tumors and cell lines show strong concordance. Maximum expression was defined as the 95th percentile value to reduce the effects of outliers. Dashed lines represent two standard deviations from the diagonal. (B) PCA of bulk tumor global gene expression profiles annotated by predicted subtypes after stepwise removal of confounding signatures. PCA figures below are colored by CD3E expression to show the influence of immune infiltration and KRT5/14 (averaged expression) to show the influence of keratinocyte-type keratins and tissue biopsy source throughout each step. Initial PCA showed a strong influence of immune infiltration and after removal of an immune correlated gene signature, PCA of the remaining gene expression reveal secondary bias from keratinocyte-type keratins likely from the skin due to overlap with primary tissue as the biopsy site. PCA of global tumor expression annotated after removal of both immune and keratin confounded genes, shows a decreased bias from immune, keratin, and the tissue biopsy site and increased similarity to cell line-clustering patterns. (C) Projection of bulk tumor expression profiles into melanoma cell line-based PCA space from Figure 1C.

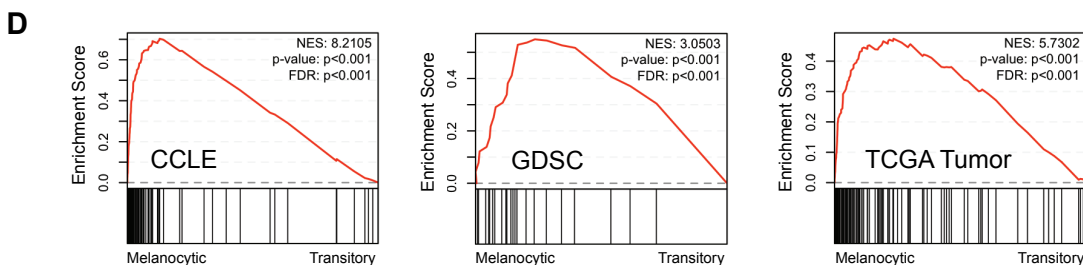
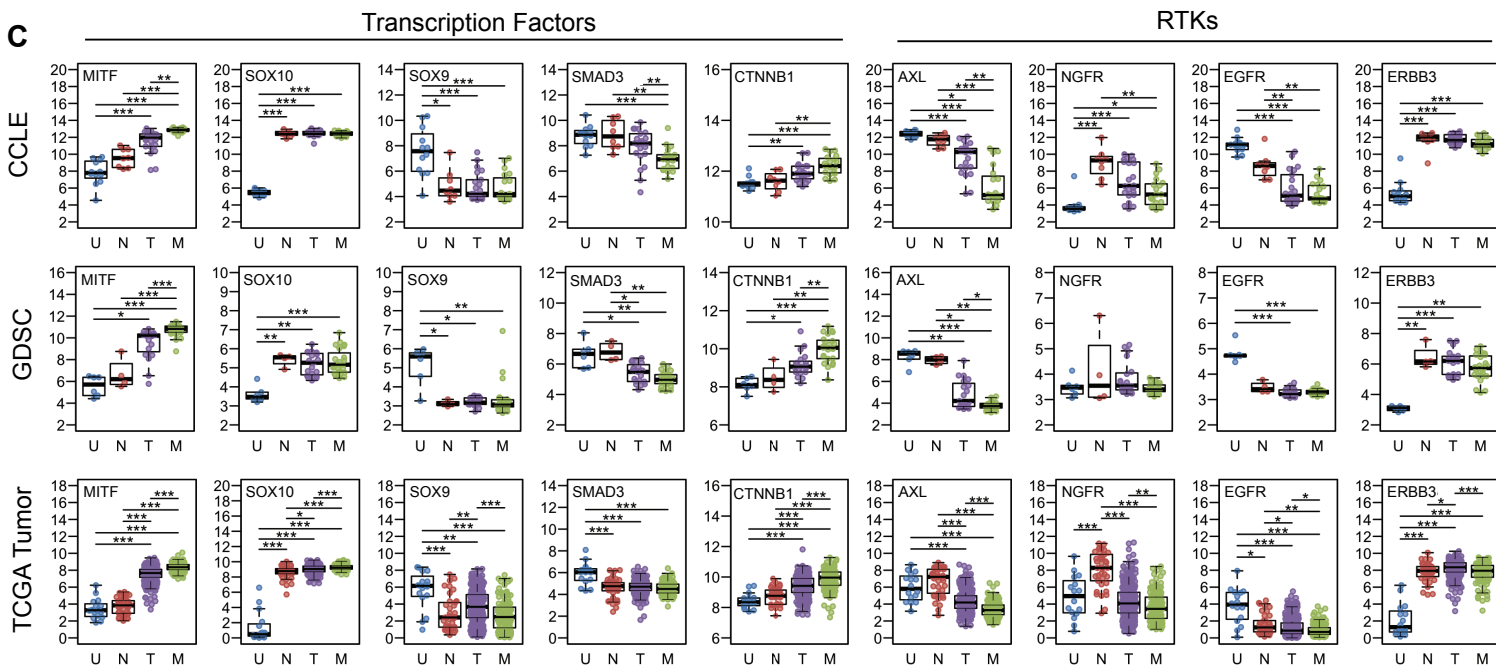
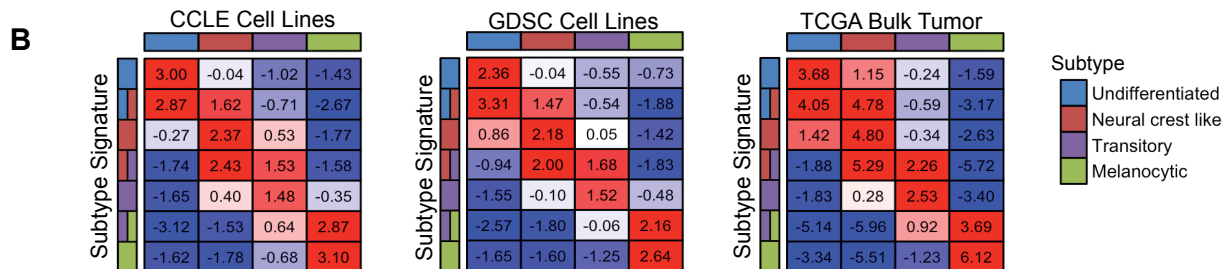
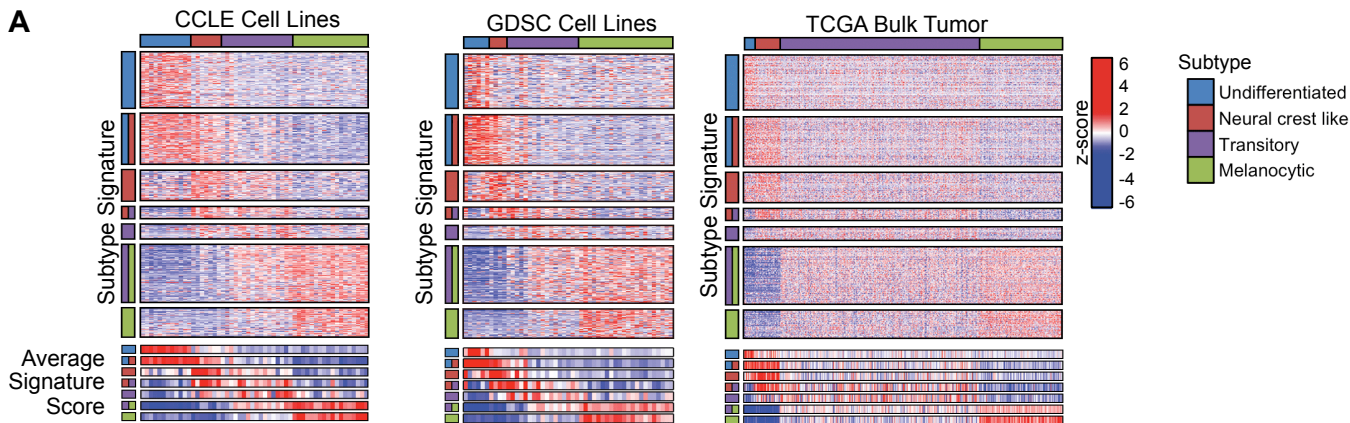


Figure S3. Differentiation marker patterns across subtypes are consistent across independent cell line and patient biopsy datasets. Related to Figure 3.

A) Heatmap of subtype signature genes (top) and average signature score (bottom) for each cell line or patient tumor samples in 3 independent datasets. (B) Heatmap of corresponding total averaged subtype scores across subtypes. To calculate the strength of each subtype signature, we calculated a score by averaging the subtype signature gene expression and then averaging all samples within a subtype set, where the average is weighted by the square root of number of samples to stabilize the variance of the mean. (C) Boxplots of select transcription factors and RTK gene expression showing their subtype-specific patterns. Boxplot lines reflect lower quartile, median, and upper quartile. Whiskers reflect 1.5 times above or below the interquartile range, with points outside reflecting outliers. (D) Enrichment analysis of Melanocytic vs. Transitory subtypes to infer MITF activity in CCLE, GDSC, and TCGA datasets. (U: Undifferentiated, N: Neural crest-like, T: Transitory, M: Melanocytic; number in each group, GDSC: U=12, N=8, T=22, M=19; GDSC: U=6, N=4, T=19, M=23; TCGA: U=16, N=37, T=294, M=123; Kruskal-Wallis ANOVA and Dunn's post hoc two-tailed test p values: * ≤ 0.05 , ** ≤ 0.01 , *** ≤ 0.001)

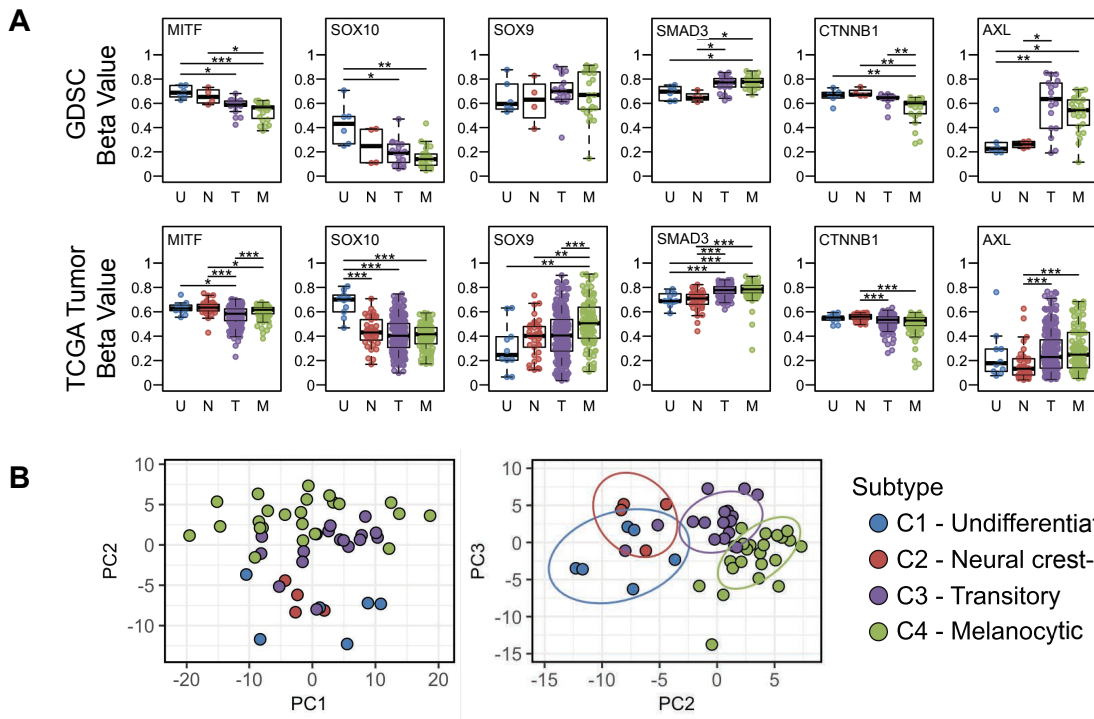


Figure S4. Epigenetic changes in DNA methylation mirror the transcriptional programs of differentiation. Related to Figure 3.

(A) DNA methylation beta values of select genes from the GDSC cell lines and TCGA tumor dataset grouped by predicted subtype. (U: Undifferentiated, N: Neural crest-like, T: Transitory, M: Melanocytic; number in each group, cell lines: U=6, N=4, T=17, M=23; tumors: U=16, N=37, T=294, M=123; Kruskal-Wallis ANOVA and Dunn's post hoc two-tailed test p values: * ≤ 0.05 , ** ≤ 0.01 , *** ≤ 0.001). Boxplot lines reflect lower quartile, median, and upper quartile. Whiskers reflect 1.5 times above or below the interquartile range, with points outside reflecting outliers. (B) PCA based on methylation beta values from the GDSC cell line dataset and annotated by predicted subtype. Plot of PC2 vs. PC3 shows subtype patterns similar to the arc-like differentiation trajectory observed with the gene expression PCA. Ellipses mark 80% confidence interval based on multivariate t-distribution. PC1 reflects another methylation signal not explained by the subtypes.

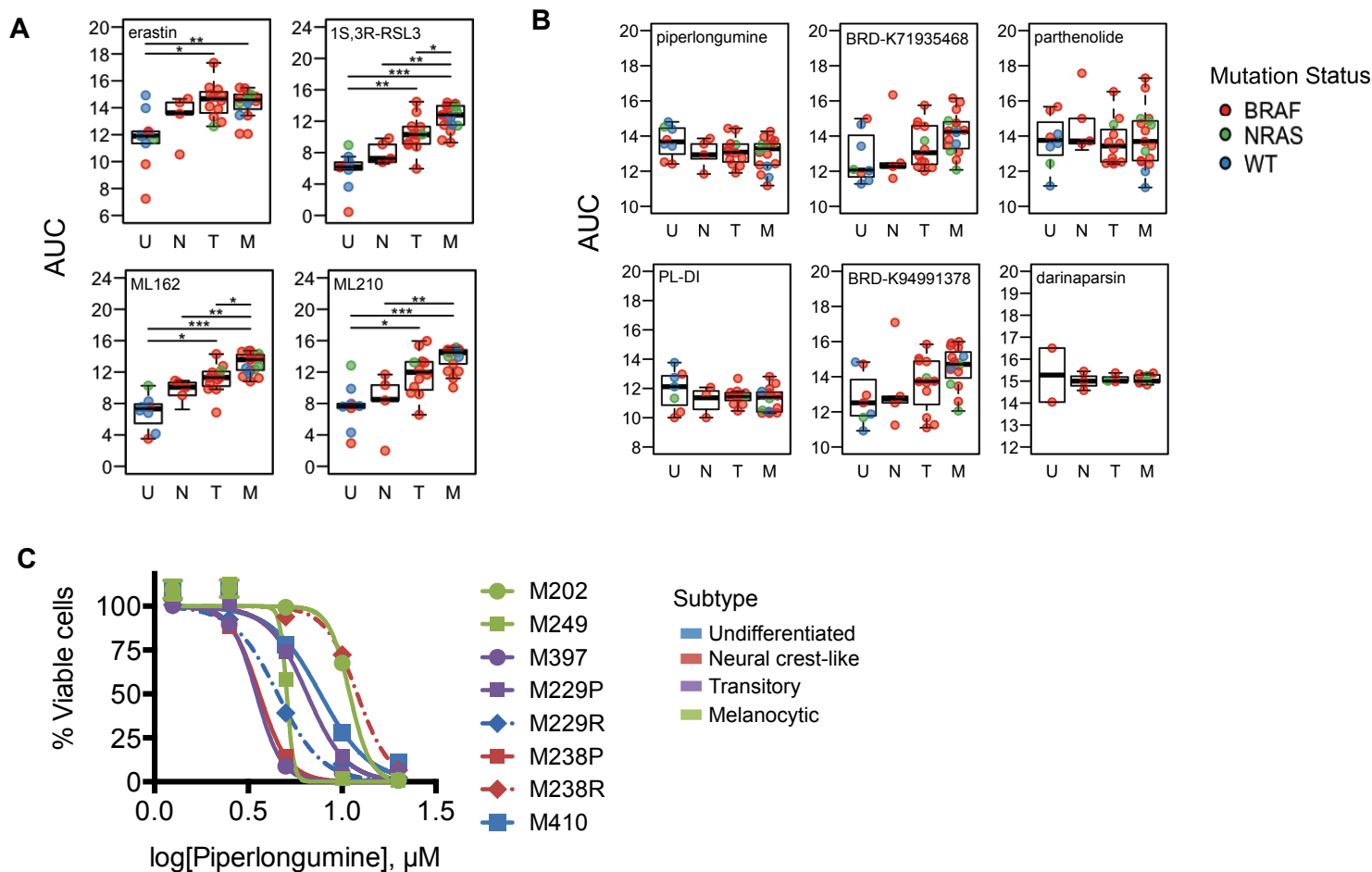
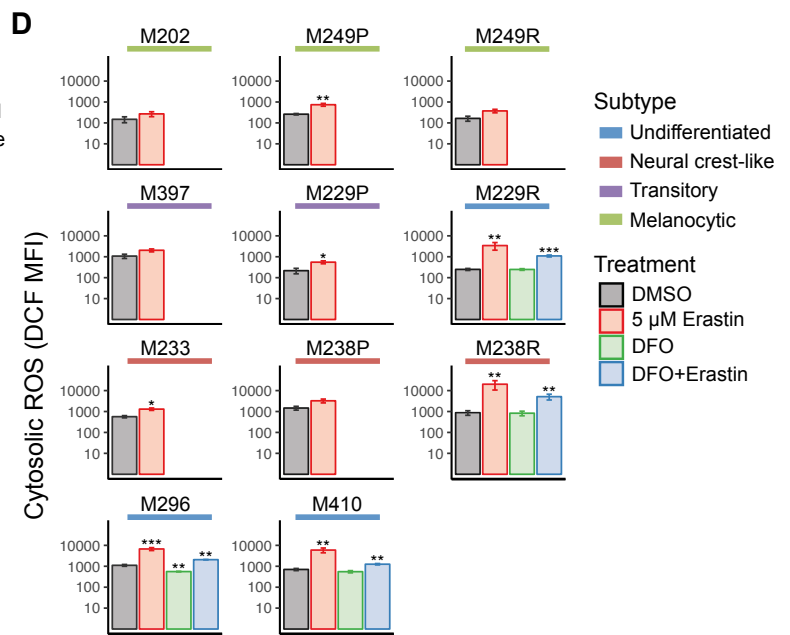
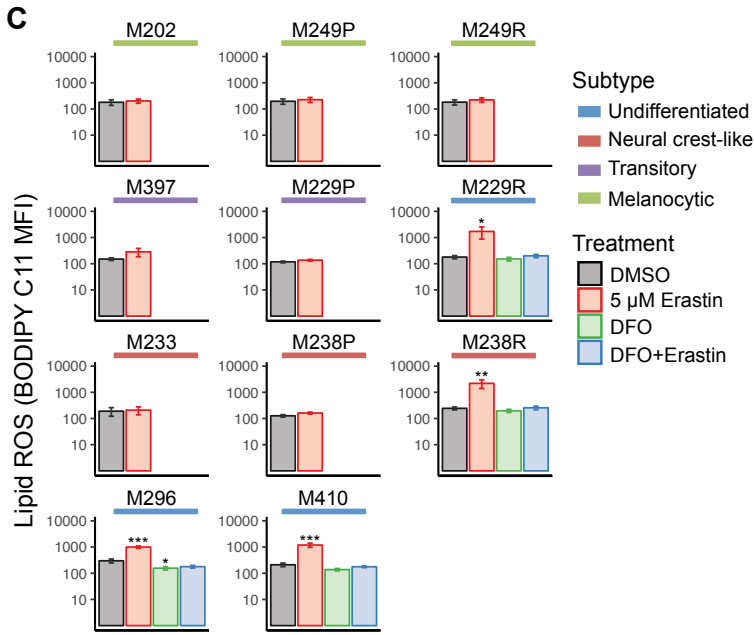
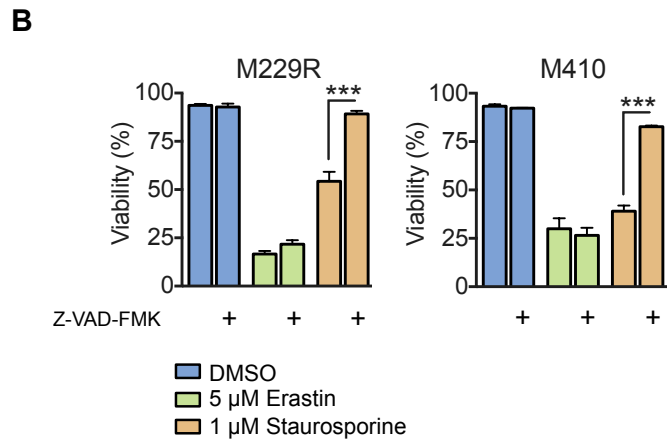
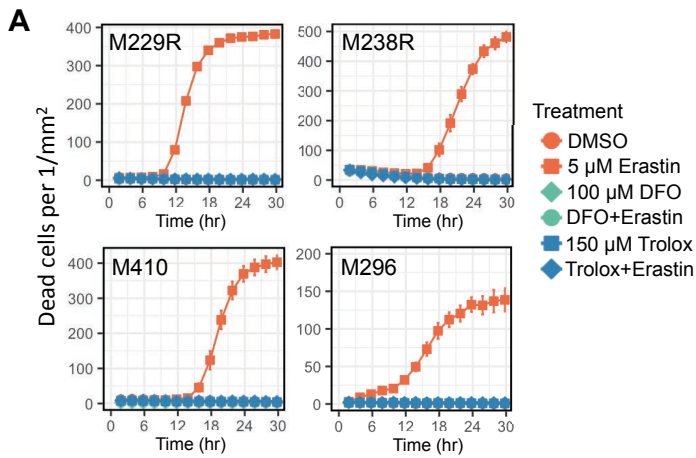
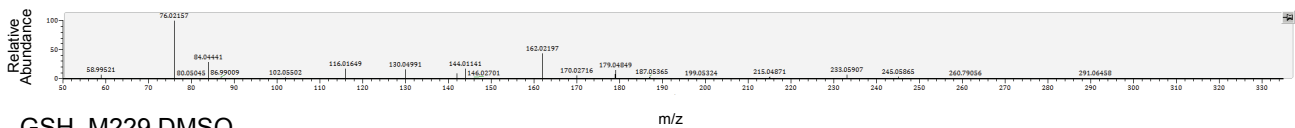


Figure S5. Sensitivity to ferroptosis inducing drugs is correlated with dedifferentiation. Related to Figure 4.

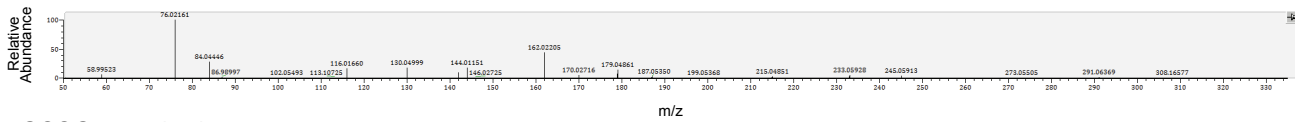
(A) Boxplot of the area under the curve (AUC) sensitivity values for the indicated ferroptosis inducing drugs grouped by predicted melanoma differentiation subtype. (B) Boxplot of AUC values from the CTRP for other ROS generating drugs that do not induce ferroptosis also do not show any distinguishable subtype trends. (U: Undifferentiated, N: Neural crest-like, T: Transitory, M: Melanocytic; Kruskal-Wallis ANOVA and Dunn's post hoc two-tailed test p values: * ≤ 0.05 , ** ≤ 0.01 , *** ≤ 0.001 , lower AUC values indicate increased sensitivity) Boxplot lines reflect lower quartile, median, and upper quartile. Whiskers reflect 1.5 times above or below the interquartile range, with points outside reflecting outliers. (C) Dose response curves showing no difference in sensitivity among subtypes and vemurafenib resistant lines when treated with the ROS-inducing (but not particularly lipid ROS-inducing nor ferroptosis-inducing) drug piperlongumine. Percent viable cells are calculated relative to DMSO. Data shown represent mean \pm sem of two replicates and representative of at least three independent experiments.



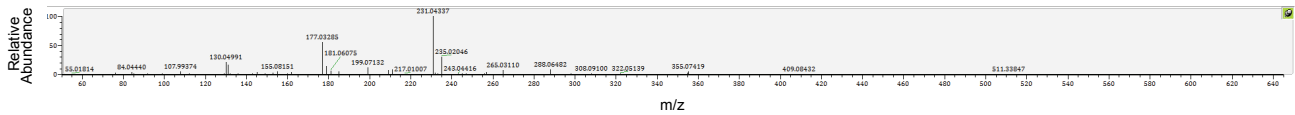
E GSH, standard



GSH, M229 DMSO



GSSG, standard



GSSG, M229 DMSO

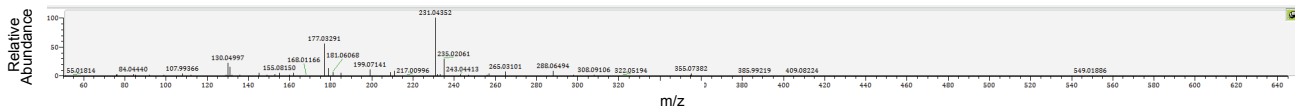


Figure S6. Confirmation of ferroptosis mechanism components in undifferentiated cell lines. Related to Figure 5.

(A) Cytotoxicity assay using the Incucyte Cytotox Red reagent showing rapid cell death with erastin treatment that can be prevented with DFO or Trolox. Data shown represent mean \pm sem of three replicates, and representative of at least three independent experiments. (B) Trypan blue exclusion assay of 24 hr erastin or staurosporine treatment with or without caspase inhibitor Z-VAD-FMK pre-treatment for 1 hr. (C, D) Mean fluorescence intensity after 10 hr erastin treatment across cell lines by flow cytometry using BODIPY-C11 probe to measure lipid ROS (C) and CM-H2DCFDA probe to measure cytosolic ROS (D). Data shown in barplots represent mean \pm sem of three independent experiments; one-tailed t-test p values: * \leq 0.05, ** \leq 0.01, *** \leq 0.001. (E) MS2 fragmentation spectrum for GSH and GSSG in a purified standard compared to representative melanoma sample. The assignments of these metabolites were based on overlapping extracted ion chromatography peak retention times and the plotted highly concordant MS2 fragmentation spectra between purified standards and samples.

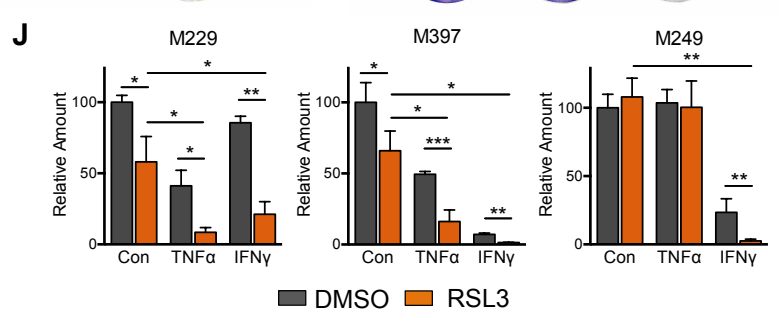
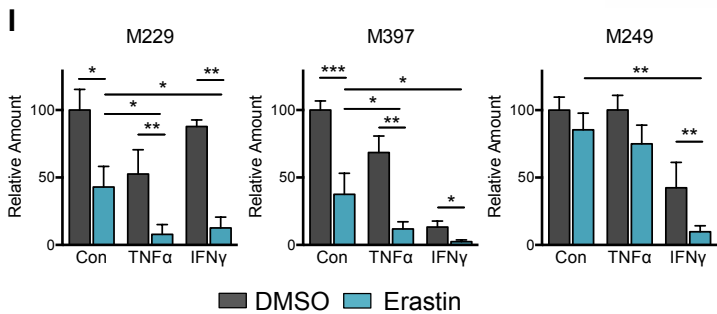
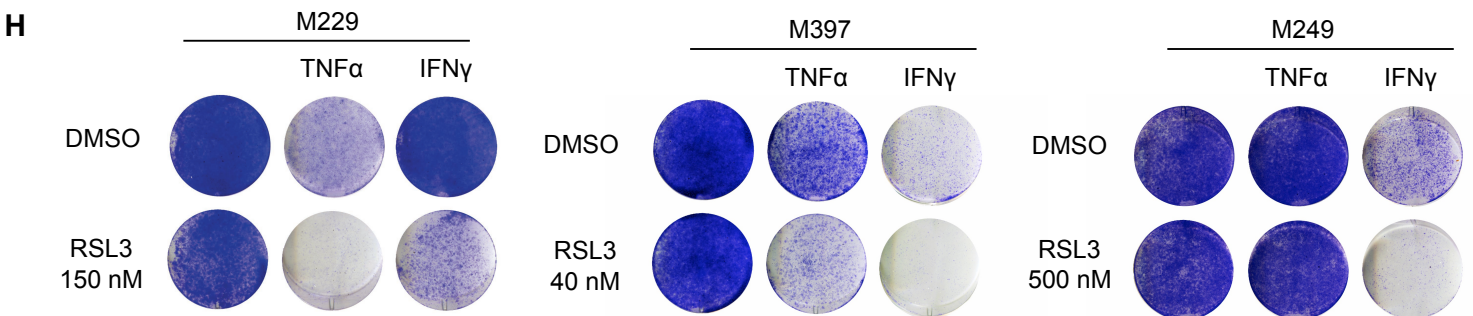
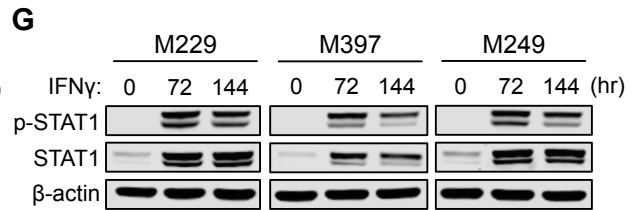
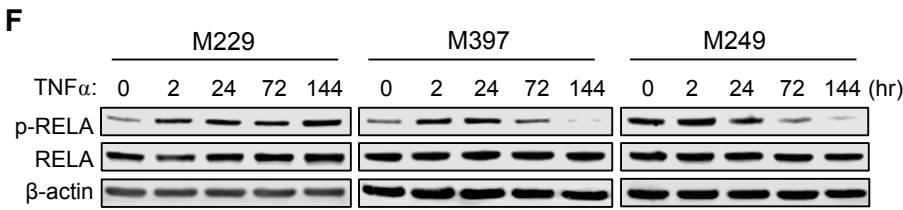
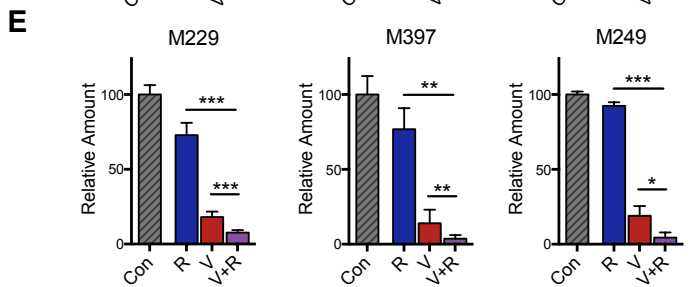
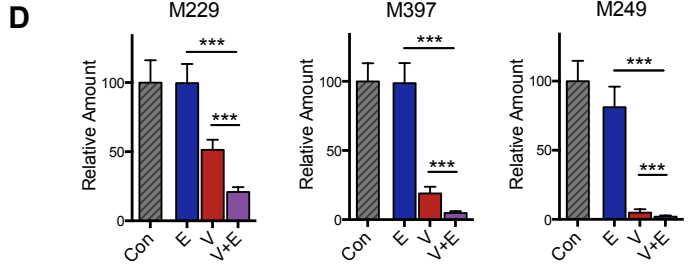
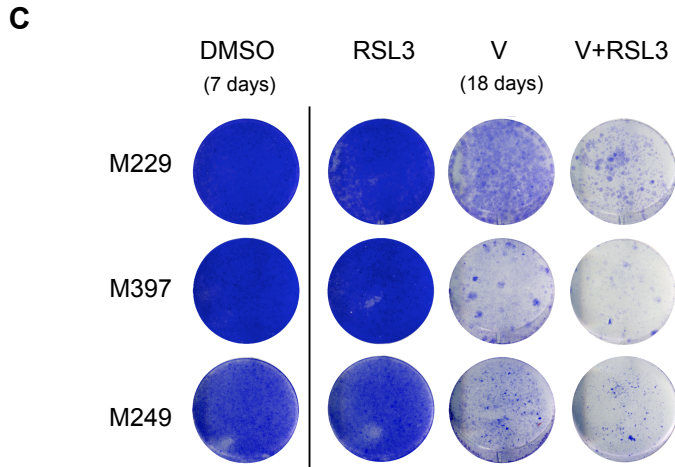
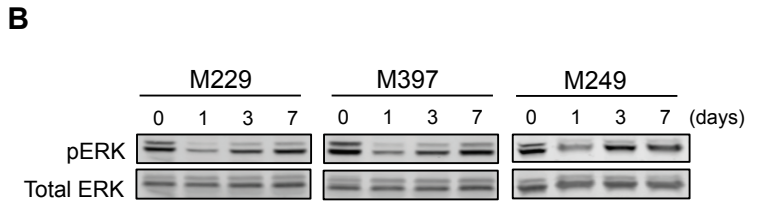
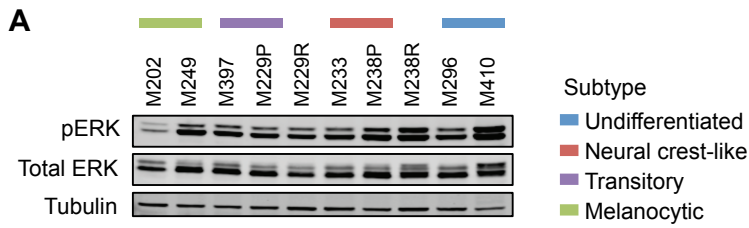


Figure S7. Reduction in persistent dedifferentiated melanoma cells upon combination treatment with RSL3. Related to Figure 7.

(A) Immunoblot of pERK (Thr202/Tyr204) levels across a panel of melanoma cell lines showing no subtype-specific patterns. (B) Immunoblot of cells treated with vemurafenib at the indicated time-points showing initial suppression and rebound of pERK. (C) Crystal violet staining assays of long-term combination treatment of RSL3 (M229: 150 nM, M397: 40 nM, M249: 500 nM) and vemurafenib (V= 1 μ M) for 21 days. DMSO treated cells were stained after 7 days. (D, E) Quantification of crystal violet staining assays testing vemurafenib in combination with erastin (D) or RSL3 (E). (F, G) Immunoblot showing confirming activation of signaling pathways by TNF α (F) or IFN γ (G) treatment. (H) Crystal violet staining assays of RSL3 treatment for 7 days with cytokine exposure for the initial 3 days (M229 and M249) or 7 days (M397). IFN γ =100 U/mL, TNF α =1000 U/mL. (I-J) Quantification of crystal violet staining assays testing cytokine exposure in combination with erastin (I) or RSL3 (J), from at least three independent experiments. Relative amounts shown for quantified crystal violet assays are normalized to the average DMSO control treatment from at least three independent experiments. Statistical tests between groups to test for decrease in persistent cells were performed using a one-tailed paired t-test. Data shown represent mean \pm sd; t-test p values: * \leq 0.05, ** \leq 0.01, *** \leq 0.001.